Unraveling catalytic properties by yttrium promotion on mesoporous SBA-16 supported nickel catalysts towards CO_2 methanation

Chao Sun[a,*], Katarzyna Świrk[b], Ye Wang[a,c], Li Li[d], Marco Fabbiani[e], Vasile Hulea[e], Magnus Rønning[b], Changwei Hu[c,d], Patrick Da Costa[a,*]

[a] Institut Jean Le Rond d'Alembert, Sorbonne Université, CNRS UMR 7190, 78210 Saint-Cyr-l'Ecole, France

[b] Department of Chemical Engineering, Norwegian University of Science and Technology (NTNU), 7491 Trondheim, Norway

[c] College of Chemical Engineering, Sichuan University, 610065 Chengdu, China

[d] Key Laboratory of Green Chemistry and Technology, Ministry of Education, College of Chemistry, Sichuan University, 610064 Chengdu, China

[e] Institut Charles Gerhardt Montpellier, UMR 5253, CNRS-UM-ENSCM, France

[*] Corresponding authors.

Email address: chao.sun@dalembert.upmc.fr; patrick.da_costa@sorbonne-universite.fr;

Abstract:

The ordered mesoporous silica SBA-16 with high specific surface area and pore volume was synthesized and used to prepare Ni/SBA-16 catalysts promoted with yttrium. These promoted catalysts were tested in CO_2 methanation reaction and characterized by N_2 sorption, small-angle/wide-angle XRD, TEM, XPS, H_2-TPR, CO_2-TPD, and TGA/DSC-MS. The results revealed that Ni/Y/SBA-16 catalysts performed better catalytic performance in CO_2 methanation compared to the non-promoted Ni/SBA-16 catalyst. The best catalytic activity was found for the catalyst promoted with 10 wt.% Y. The improved performance of such catalysts was attributed to the increase of reducibility of nickel species, the increase in surface oxygen species, and the abundance of moderate basic sites caused by Y promotion. Furthermore, the CO_2 reaction rate and turnover frequency of CO_2 were

well correlated with the number of moderate basic sites. Finally, all the tested catalysts are highly stable during the 8h time-on-stream catalytic test.

Keywords: CO_2 methanation, synthetic natural gas, Ni catalyst, SBA-16, yttrium promotion

1. Introduction

Over the last decades, industrialization and urbanization across the world have led to a significant increase in carbon dioxide (CO_2) emissions, well known as the main greenhouse gas (GHG) leading to global warming [1]. According to the World Meteorological Organization (WMO) report from 2020, then anthropogenic CO_2 emission had risen by about 1% annually over the last decade, resulting in an increase of CO_2 concentration between 2 and 3 ppm in the atmosphere. The consequences of this global warming are mostly desertification, rising sea levels, and animal species extinction [1]. Therefore, the reduction of CO_2 emissions is one of the most important challenges for modern societies. Although in the last years, renewable energies have been used to reduce CO_2 emission, the dependence on fossil fuels still cannot be relieved in short term. In such a case, the development of technologies to reduce CO_2 emission directly from the source can be of importance. The CO_2 capture and utilization (CCU) technology, which captures the CO_2 and uses it as feedstock to produce fuel, can play a significant role in CO_2 reduction [2]. In this technology, the power-to-gas (PtG) route is regarded as a mature route because it can convert intermittent renewable energy to synthetic natural gas [3,4]. CO_2 methanation,

which was for the first time reported by Paul Sabatier in 1902 [5,6], plays a key role in the PtG concept. In this concept, the captured CO_2 reacts with the hydrogen originated from the water electrolysis by renewable energy, such as wind, solar, or hydropower to synthesize methane (CH_4) [4]. In this regard, the fluctuant renewable energy can be stored in the form of CH_4, which can be easily transported or injected into the existing gas pipelines [3]. Compared to other CO_2 conversion reactions like methanol, dimethyl ether, and formic acid, etc. [7,8], CO_2 methanation possesses many advantages, such as high activity and selectivity, low cost, and high energy efficiency [4,9]. CO_2 methanation is a moderate reaction that can be performed at ambient temperature. The energy conversion efficiency from electricity to methane can reach 63.6% [4]. CO_2 methanation is also a thermodynamically feasible and exothermic reaction, determined with the equation:

$$CO_2 + 4H_2 \rightarrow CH_4 + 2H_2O \ (\Delta H_{298K} = -165 \ kJ \bullet mol^{-1}) \qquad \text{Equation (1)}$$

However, this reaction needs the presence of an appropriate catalyst due to the restriction of the kinetic barrier. The transition metal-based catalysts, such as Rh [10], Ru [11], Pd [12], Ni [9,13], Co [14], were widely used to catalyze this reaction. Among these catalysts, the noble catalysts including Rh and Ru can catalyze the reaction at a temperature lower than 200 C° [15,16]. However, the high cost and low availability limit their potential large-scale commercialization. Meanwhile, Ni-based catalysts have already received intensive attention due to their high performance and low price [17]. Among them, Ni catalysts supported on various supports, such as CeO_2 [18–20], Al_2O_3 [21], SiO_2 [22–24], ZrO_2 [25], $Ce_xZr_{1-x}O_2$ [26], TiO_2 [27], mesoporous silicas [9,28,29], perovskite [30], and hydrotalcite-derived mixed oxides [31–36], always showed higher activity due to the beneficial effect of the used supports. The support plays an important role in the catalytic systems, allowing

to improve surface area and porosity [37,38], nickel dispersion [39], nickel particle size distribution [40], basicity [38], reducibility [41], oxygen vacancies [13,42], and metal-support interaction [43,44]. The above-mentioned properties can significantly affect the activity and stability of Ni catalysts.

Mesoporous materials with highly ordered structures have been utilized as supports for Ni catalysts due to their high surface area, porosity, and unique ordered structure [9,29,45–49]. For CO_2 methanation, Bacariza et al. [49] compared the performance of Ni catalysts supported on SBA-15, MCM-41, and USY zeolite. The results revealed that the Ni/MCM-41 catalyst showed the highest turnover frequency (TOF) values, which was due to weakened poisoning effects of carbonyl species. The Ni metal particle size on SBA-15 was lower due to the bigger pore size than that on MCM-41. It was also found that the incorporation of cerium could notably increase the activity of Ni catalysts supported over different supports. Guo et al. [50] prepared Ni catalysts supported on ZSM-5, SBA-15, and MCM-41 by wet impregnation method and compared their performance in CO_2 methanation with conventional Al_2O_3 and SiO_2 supported catalysts. The Ni catalysts supported on ZSM-5 and SBA-15 showed superior activities than alumina and silica-supported catalysts. The higher performance of Ni/ZSM-5 was assigned to the enhanced basic properties and the synergistic effect between nickel metal and support. To further improve the catalytic activity of mesoporous supported Ni catalysts, promoters such as La [48,51], Mg [9], and Ce [52] were also applied. The promotion with Ce usually leads to an increase of the oxygen vacancies on the catalyst due to its redox property (Ce^{4+}-Ce^{3+}), which can promote the adsorption and dissociation of CO_2 [53–55]. Besides, the presence of Ce on Ni/SBA-15 catalysts led to the decrease of Ni particle size [56,57]. The

incorporation of lanthanum could promote Ni dispersion due to the intensified interaction La-Ni and the adsorption and activation of CO_2 [48]. Meanwhile, the modification with Mg was found to increase medium basic sites, which can promote monodentate formate species during methanation reaction [9]. However, both MCM-41 and SBA-15 are 2-dimensional mesoporous materials that may have contributed to some extent to the remarkable sintering of Ni° particles [58,59]. In this regard, 3-dimensional material, such as SBA-16 could be an interesting alternative due to the possible confinement of active metals, leading to high stability in long time running [47,60–63]. SBA-16 has been already reported to be promising support, allowing to obtain small Ni particle size due to its cage-like mesoporous structure [64]. Regarding CO_2 methanation, only a few studies dealt with SBA-16 based catalysts. Canggih et al. [64] investigated Ni/SBA-16 catalysts in CO_2 methanation and found that the Ni particle size was very small due to the confinement of SBA-16. However, the activity and CH_4 selectivity of Ni/SBA-16 catalysts in CO_2 methanation were not ideal due to the lack of basicity. Chen et al. [60] applied carboxylic acid-modified SBA-16 based Ni catalysts in CO_2 methanation, but the reported activity was not ideal compared to the other catalysts. Recently, it has been demonstrated that the presence of ceria as a promoter could significantly enhance the activity of Ni/SBA-16 catalysts [25]. Besides ceria, yttrium can also be a good promoter. It has been widely reported that the modification with yttrium can promote the activity of Ni catalysts supported on different materials in various CO_2 valorization reactions including CO_2 methanation [13,31,65,66]. Moreover, the yttrium has more available ore deposits compared to other rare earth elements (REEs), making it potential in large-scale application towards CO_2 utilization [67]. Yttrium have demonstrated positive effects on Ni catalysts supported on different materials

120 [13,19,30,31]. Regarding the effect of yttrium on mesoporous silica supported Ni catalysts,
121 several researches focused on methane reforming of CO_2 reaction [68,69]. However, few
122 studies dealt with Ni catalysts supported on mesoporous silicas promoted with yttrium
123 applied in CO_2 methanation. In previous studies, we found that the presence of Y could
124 significantly improve the activity of hydrotalcite-derived and SBA-15 supported Ni
125 catalysts [31,70]. However, the effect of Y on Ni catalyst supported on SBA-16 material
126 has never been reported. Herein, we studied the effect of Y on Ni/SBA-16 catalysts for
127 CO_2 hydrogenation to methane.

128 In this study, Ni/SBA-16 catalysts promoted by different loadings of yttrium were
129 synthetized and further investigated their activity and stability in CO_2 methanation. The
130 catalysts were characterized by a temperature-programmed reduction in H_2 (H_2-TPR),
131 temperature-programmed desorption of CO_2 (CO_2-TPD), N_2 physisorption, small-angle
132 and wide-angle X-ray diffraction (SAXRD and WAXRD), high-resolution/transmission
133 electron microscopy (TEM/HRTEM), energy-dispersive X-ray spectroscopy (EDS), X-ray
134 photoelectron spectroscopy (XPS), and thermogravimetric analysis/differential scanning
135 calorimetry-mass spectrometer (TGA/DSC-MS). Finally, a relation between activity and
136 physicochemical properties was drawn.

137

138 # 2. Experimental part

139 ## 2.1. Catalyst preparation

140 2.1.1. SBA-16 synthesis

141 The SBA-16 materials were synthesized based on an improved method presented
142 elsewhere [71]. Typically, 3 g of Pluronic F127 ($EO_{106}PO_{70}EO_{106}$) copolymer (BASF) was
143 dissolved with 144 g of distilled water in a Teflon bottle followed by adding 5.94 g of
144 concentrated hydrochloric acid (HCl, 37 wt.%, Sigma Aldrich). After stirring for 30 min,
145 9 g of butanol-1 (BuOH, Sigma Aldrich) was added into the aforementioned solution as a
146 co-surfactant. The molar ratio of F127:BuOH was chosen as 1:3. After stirring for 1 h, 14.2
147 g of tetraethyl orthosilicate (TEOS, Sigma Aldrich) was added into the solution above at
148 40°C, then the mixture was kept at 40°C for 24 h. Afterward, the container of the solution
149 was placed under a static condition at 80 °C for 48 h for the hydrothermal process.
150 Subsequently, the mixture was filtered and washed with distilled water. Then, the
151 precipitant was dried at 100 °C for 12 h. Finally, the solid was calcined at 550 °C for 5 h
152 with a heating rate of 5 °C/min under flowing air (20 mL/min) to remove the copolymer
153 template F127.

154

155 2.1.2. Ni catalysts preparation

156 The Ni/xY/SBA-16 catalysts were prepared by a two steps impregnation method. The as-
157 synthesized SBA-16 material was used as support.

158 First, Y-modified SBA-16 (xY/SBA-16) was synthesized by impregnating an aqueous
159 solution of yttrium nitrate ($Y(NO_3)_3 \cdot 6H_2O$, >99%, Sigma-Aldrich) onto the support.
160 Typically, the appropriated weight of $Y(NO_3)_3 \cdot 6H_2O$ was dissolved in distilled water. Then,
161 2 g of SBA-16 was added into the above-mentioned solution followed by the treatment in
162 an ultrasonic bath (Elmasonic S30) for 1.5 h to obtain a well-dispersed suspension.

Subsequently, the suspension was placed in static condition for 24h for the impregnation part. Afterward, the container was placed in an oven at 100°C for 12h. After drying, the solid was grounded and calcined at 550°C for 5h with a heating rate of 5°C/min. The weight percent of Y relative to SBA-16 was adjusted to 5, 10, and 20 wt.%.

The synthesized xY/SBA-16 supports were used to synthesize Ni/xY/SBA-16 catalysts by wet impregnation using nickel nitrate ($Ni(NO_3)_2 \cdot 6H_2O$, >99%, Sigma-Aldrich). The procedure was nearly the same as the process of xY/SBA-16 with the use of ethanol (99.9%, Sigma-Aldrich) instead of distilled water. The nickel loading relative to SBA-16 was 10 wt.% for all the samples. The synthesized catalysts were denoted as: 10Ni/SBA-16, 10Ni/5Y/SBA-16, 10Ni/10Y/SBA-16, and 10Ni/20Y/SBA-16. The schematic diagram was displayed in Scheme 1.

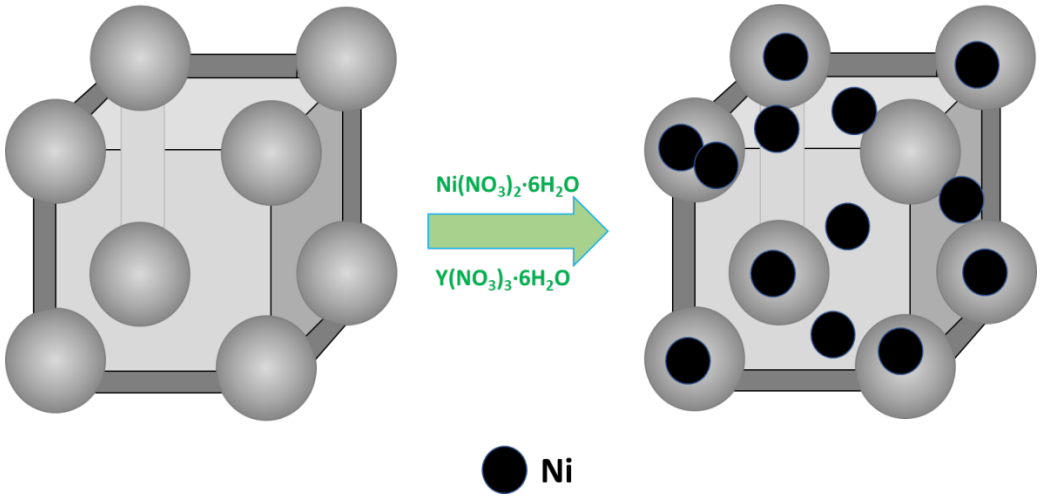

Scheme 1. Schematic diagram of the morphology of SBA-16 and Ni/SBA-16 catalyst.

2.2. Physicochemical characterization

178 N_2 physisorption isotherms were obtained on a TriStar 3000 Micromeritics apparatus.
179 Before N_2 adsorption, the sample was degassed at 300 ℃ under vacuum conditions for 3 h
180 [72]. After the pretreatment, the N_2 adsorption-desorption experiment was carried out
181 under liquid nitrogen temperature (-196 °C) [73]. The specific surface area (SSA) was
182 calculated by the Brunauer-Emmett-Teller (BET) method. The total pore volume (V_p) and
183 mean pore size (r_p) were calculated by the Barrett-Joyner-Halenda (BJH) method.

184 The wide-angle X-ray diffraction (XRD) experiments were performed on a PANalytical-
185 Empyrean diffractometer equipped with a Cu Ka radiation source (λ = 0.15406 nm, 40 kV,
186 40 mA). The patterns were recorded from 10 to 90° with a step of 0.02° (2θ). The crystallite
187 size of nickel species was calculated by the Scherrer equation (2):

188 $$D_{hkl} = \frac{K\lambda}{\beta_{hkl} cos\theta} \quad \text{(Equation 2)}$$

189 In which k is the Scherrer parameter (0.9); λ is the radiation wavelength (λ=0.15406 nm),
190 β_{hkl} refers to the full width at half maximum (FWHM) of the reflection peak, and θ
191 represents the Bragg diffraction angle.

192 The small-angle X-ray scattering (SAXS) patterns were obtained in the range 0.5-5.0° with
193 a step of 0.01° (2θ) on a Bruker D8 instrument using Cu Ka radiation (λ=1.5406Å) on a
194 silicon sample holder. The structural parameter of d_{110} was acquired from the XRD
195 diffractogram by using the Jade 6.5 software. The a_0 and h were calculated by $a_0=2d_{110}/\sqrt{3}$
196 and $\sqrt{3}/2 \times a_0 - D$, respectively [74].

197 Transmission electron microscopy (TEM), High-resolution transmission electron
198 microscopy (HRTEM), and Energy Dispersive X-ray spectroscopy (EDX) experiments
199 were carried out in a JEM-2010 UHR (JEOL, Tokyo, Japan) equipment for reduced

200 catalysts. Before analysis, the catalyst was reduced at 500 °C for 1.5 h in a mixture of
201 5%H_2/Ar. Afterward, the catalyst was dispersed in ethanol solution and added dropwise on
202 a copper grid covered by carbon film. Finally, the prepared specimen was used for the
203 microscopy analysis.

204 D_{Ni} (%) is the Ni dispersion calculated by TEM measurement as shown in Eq. 4. It assumes
205 that the Ni particle is hemispherical, in which V_M is the bulk atomic volume (1.09×10^{-23}
206 cm^3) and A_M is the Ni atomic area (6.51×10^{-16} cm^2), and the surface-weighted average
207 diameter d_{sw} (nm) were calculated by Eq. 3 [75]. The d_i and N_{di} represent the diameter of
208 the particle and the number of particles with a diameter of d_i, respectively.

209 $$d_{sw} = \frac{\sum_n^{i=1} N_{di}\, d_i^3}{\sum_n^{i=1} N d_i\, d_i^2} \qquad \text{Equation (3)}$$

210 $$D_{Ni}\ (\%) = 6\times10^9 \frac{V_{Ni}}{A_{Ni}} . \frac{1}{d_{sw}} = \frac{mol\ of\ surface\ Ni\ atoms}{m_{cat} \cdot W} \qquad \text{Equation (4)}$$

211 In which, m_{cat} represents the weight of catalyst in reaction; W is the weight percent of Ni.

212 X-ray photoelectron spectroscopy (XPS) analyses were conducted in an AXIS Ultra DLD
213 spectrometer from KRATOS with a radiation from a monochromatic Al source (Al-Kα, 15
214 kV, 10 mA, 150 W). Prior the test, the sample was reduced under H_2/Ar gas mixture (5%;
215 100 mL/min) at 500 °C for 1.5 h. After cooling down to ambient temperature the same gas
216 mixture, the sample was placed in the sample chamber for the XPS test. The spectra were
217 recorded at room temperature under high vacuum conditions. The registered spectra were
218 calibrated by the C1s peak at 284.6 eV originating from the contamination during the
219 preparation of the sample.

The reducibility of the catalysts was measured by temperature-programmed reduction in H_2 (H_2-TPR) conducted on a BELCAT-M apparatus from BEL Japan Inc, which was equipped with a thermal conductivity detector (TCD). Prior measurements, the sample (60 mg) was treated in pure helium (He, 50 mL/min) at 350 °C for 1 h for impurities removal. Afterward, the sample was cooled to 50 °C before being filled by a mixture of H_2/Ar (v/v: 5%, 50 mL/min) for 20 min. Thereafter, the sample was heated from 50 °C to 900 °C with a temperature ramp of 10 °C/min under the same gas mixture. The pure bulk copper oxide (CuO) was used as a reference for H_2 consumption.

The basicity of the catalyst was carried out by temperature-programmed desorption of CO_2 (CO_2-TPD) performed in the same set-up as H_2-TPR. Before measurement, a sample of 60 mg was reduced in a 5% H_2/Ar gas mixture (50 mL/min) at 500 °C for 1.5 h. Afterward, the sample was cooled down to ambient temperature under the same gas flow following by the blow of pure He for 15 min (50 mL/min). After that, the same sample was saturated by a 10% CO_2/Ar gas mixture (50 mL/min) for 1 h. After adsorption of CO_2, the sample was flushed with He (50 mL/min) for 30 min to desorb the physically adsorbed CO_2. The TPD program was carried out in He (50 mL/min) from 50 to 900 °C with a heating rate of 10 °C/min.

Thermogravimetric analysis coupled with differential scanning calorimetry and mass spectrometry (Netzsch STA 449C Jupiter, MS: Netzsch Aëolos QMS 403C) was conducted to analyze possible coke deposition on the catalyst after methanation. The spent catalyst was heated in a temperature range of 35-900 °C with a heating ramp of 5°C/min in the air (55 ml/min) with a simultaneous recording of products formed during decomposition (mass-to-charge ratio, CO_2: m/z = 44; H_2O: m/z=18).

2.3 Catalytic performance test in CO_2 methanation

The catalytic performance in CO_2 methanation was evaluated in a static tubular quartz reactor (U-type, inner diameter: 8 mm) under 1 atm. The catalyst was heated by a temperature-programmed electric furnace equipped with a K-type thermocouple positioned near to the catalyst bed (<1mm) to record the temperature. Before the catalytic test, the sample (0.5 mL) was pretreated in an H_2/Ar gas mixture (v/v: 5%; Flow rate: 100 mL/min) from ambient temperature to 500 °C and kept for 1.5 h with a temperature ramp of 10 °C/min. After pretreatment, the sample was cooled down to 200 °C and feed gas mixtures (CO_2/H_2/Ar = 15/60/25, 100 mL/min) were fed into the sample with a gas hourly space velocity (GHSV) of 12,000 h^{-1}. The products of the outlet were analyzed by a gas chromatograph from Agilent (490 Varian) equipped with a thermal conductivity detector (TCD). The flow rates in the inlet and outlet of the reactor were controlled by mass flow controllers (5850TR, Brooks) and the actual flow rates were measured by a soap-film flowmeter placed at the outlet. The reaction temperature was controlled in the range of 200-450 °C with a step of 50 °C. The reaction was kept at least for 30 minutes at each temperature to reach a steady state. The products after reaction recorded by GC were CH_4 and CO (the only by-product). CO_2 conversion and CH_4 selectivity were calculated by the following equations (5) and (6):

$$XCO_2(\%) = \frac{FCO2,_{in} - FCO2,_{out}}{FCO2,_{in}} \times 100\% \qquad \text{Equation (5)}$$

$$SCH_4(\%) = \frac{FCH4,_{out}}{FCH4,_{out} + FCO,_{out}} \times 100\% \qquad \text{Equation (6)}$$

where X indicates CO_2 conversion; S represents CH_4 selectivity; $F_{CO2,in}$ and $F_{CO2,out}$ are the molar flow rate of CO_2 with “in” and “out” referring to the inlet and outlet, respectively;

$F_{CH4,out}$ and $F_{CO,out}$ represents the molar rate of CH_4 in the outlet. The molar flow rate was calculated based on the volumetric flow rate and the compositions from the GC.

The CO_2 methanation reaction rate (r_{CO_2}) was calculated using the following equation (7) [75]:

$$r_{CO_2} = \frac{F_{CO_{2,in}} \times X_{CO_2}}{W} \quad \text{Equation (7)}$$

in which r_{CO2} is the reaction rate ($mmol \cdot g_{cat}^{-1} \cdot min^{-1}$); $F_{CO2,in}$ represents the CO_2 molar flow rate ($mol \cdot min^{-1}$); X_{CO2} is the CO_2 conversion; W represents the weight of catalyst (g).

At 300°C, the turnover frequency (TOF, Eq. 8) was calculated based on the literature [9], representing the mole of CO_2 converted per mole of surface nickel atoms per second.

$$\text{TOF } (s^{-1}) = \frac{X_{CO_2} \times F_{CO_{2,in}}}{mol\ of\ surface\ Ni\ atoms} \quad \text{Equation (8)}$$

In which, the X_{CO2} and $F_{CO2,in}$ are the same as those in equation (5), the mole of surface Ni atoms was measured based on TEM as depicted in equation (4).

2.4 Stability test in CO_2 methanation

Stability tests were carried out in the same experimental setup as described in section 2.3. The sample of 0.5 mL was reduced at the same conditions introduced in the catalytic test part (See 2.3) following cooling down to 350 °C for the stability test at the same conditions as stated before. The time-on-stream (TOS) experiments were conducted for 8 h at 350 °C. The temperature of 350 °C was selected due to distinguishable CO_2 conversion values of

284 catalysts performed in the catalytic test at this temperature. CO_2 conversion and CH_4
285 selectivity were calculated by equations (5) and (6), respectively.

286

287 3. Results and discussion

288 3.1 Catalytic performance of the Y-promoted Ni/SBA-16 catalysts in CO_2
289 methanation

290 The catalytic performance of the studied catalysts was evaluated in CO_2 methanation as a
291 function of temperature from 200 to 450 °C. The CO_2 conversion and CH_4 selectivity of
292 catalysts are presented in **Fig.1a, b.** The thick black lines in **Fig.1a** and **Fig.1b** represent
293 the thermodynamic simulation of CO_2 conversion and CH_4 selectivity, respectively. It can
294 be seen that doping Y of 10 wt.% significantly improved the CO_2 conversion of Ni/SBA-
295 16 catalyst at 300-350℃ range. Also, one can be noted that Y promoted the CH_4 selectivity
296 of Ni/SBA-16 catalyst in the temperature range of 250-350℃ (**Fig.1b).** The catalyst
297 containing 10 wt.% of Y showed the highest CO_2 conversion and CH_4 selectivity in the
298 studied temperatures. 10Ni/10Y/SBA-16 catalyst tested at 350℃ revealed 68.2% of CO_2
299 conversion and 94.8% of CH_4 selectivity. Also, one can note that at 450°C, the conversions
300 of CO_2 reached the Thermodynamics with the experimental error.

301 In order to explain the promotion effect of Y on Ni/SBA-16 catalyst, the physicochemical
302 properties of the support and catalysts were obtained and correlated to the activity in the
303 next section.

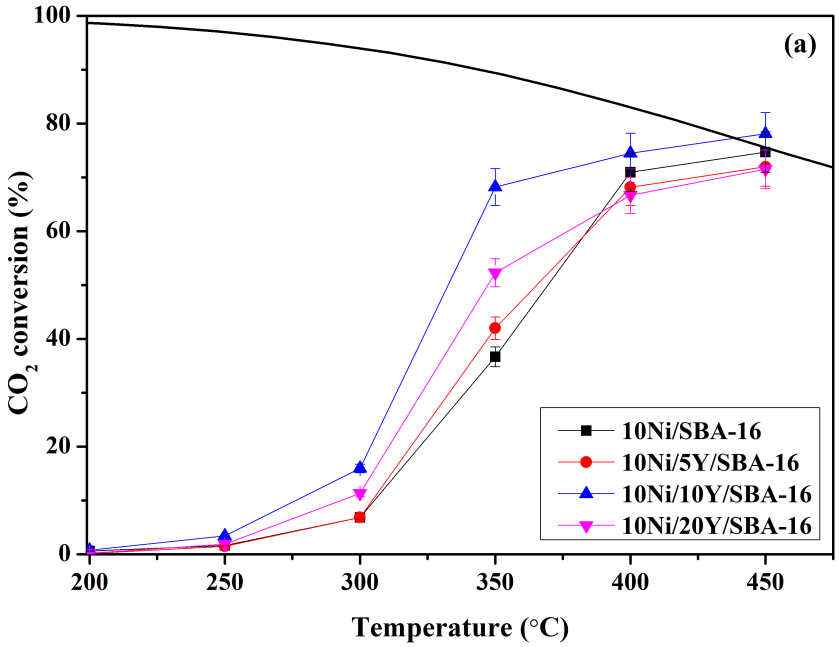

304

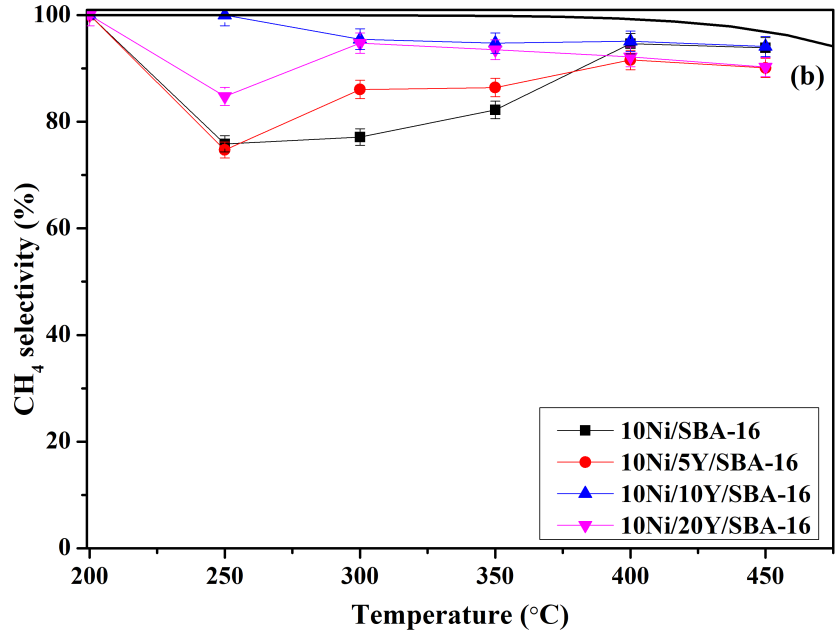

305

306 **Figure. 1.** Catalytic results of Ni/Y/SBA-16 studied in CO_2 methanation; (a) CO_2 conversion, (b) CH_4
307 selectivity, $CO_2/H_2/Ar$=15/60/25, Total flow 100 mL.min^{-1}, The solid line corresponds to the
308 thermodynamic equilibrium.

309

3.2 Textural properties, structural properties, morphology, and surface element compositions of the catalysts

N_2 adsorption-desorption experiments were conducted for the SBA-16 material, unpromoted Ni/SBA-16, and Ni/Y/SBA-16 catalysts. The isotherms of calcined samples are presented in **Fig.2**. All samples showed a type IV isotherm based on the IUPAC classification with a typical type of H_2 hysteresis loop, indicating that the mesoporous structure is still present after the introduction of Ni and Y. Also, the capillary condensation was found at relative pressures (p/p^o) of 0.45-0.85 for all samples, which demonstrated the presence of large, uniform, cage-like mesopores [71,76]. After the Ni introduction, the height and width of the hysteresis loop of Ni/SBA-16 decreased compared to SBA-16 material, indicating a decrease in pore volume [76]. Also, as shown in **Table 1**, the SSA and V_p decrease compared to those of SBA-16, which corresponds to the deposition of Ni inside the mesopores. For Y-doped catalysts, as the increase of Y loading, the height and width of the hysteresis loop of Ni/Y/SBA-16 catalysts also show decreased trends, indicating the possible presence of Y inside the mesopores.

The pore size distribution curves calculated by BJH on the desorption isotherms are displayed in **Fig.S1**. As depicted in **Fig.S1**, the pore size distribution of all samples is between 3 and 4 nm. The presence of Y has an insignificant effect on the primary pore size of Ni/SBA-16 catalyst as reported in **Table 1**. The SSA and pore volume (V_p) of Ni/SBA-16 decreased largely after modification with Ni compared to the bare support. This indicates that Ni has been deposited inside the mesopores, which is also confirmed in other reports [47]. SSA and V_p of Ni/Y/SBA-16 catalysts decreased with the increasing Y loading as a result of clogging of pores by both nickel and yttrium.

Table 1 Textural properties, structural parameters, and Ni crystallite size of the catalysts.

Catalyst	SSA (m^2/g)[a]	V_p (cm^3/g)[b]	D (nm)[b]	Structure Parameter (nm)			Crystallite size (nm)[f]		Average Ni particle size (nm)[g]	D_{Ni} (%)[g]
				d_{110}[c]	a_0[d]	H[e]	NiO	Ni^0	Ni^0	
SBA-16	996	0.77	3.4	9.945	11.6	6.6	-	-	-	-
10Ni/SBA-16	675	0.63	3.4	9.934	11.4	6.5	4.0	4.9	9.4	9.3
10Ni/5Y/SBA-16	514	0.5	3.4	9.589	11.1	6.2	14.6	12.1	19.9	4.2
10Ni/10Y/SBA-16	462	0.47	3.5	10.099	11.7	6.6	17.5	13.0	21.0	3.2
10Ni/20Y/SBA-16	343	0.39	3.6	9.878	11.4	6.3	17.8	13.7	24.5	3.3

[a] Calculated by the BET method.

[b] Calculated from BJH desorption cumulative volume and BJH Desorption average pore width (4V/A).

[c] Obtained from SAXS.

[d] calculated from the $a_0=2d_{110}/\sqrt{3}$

[e] Wall thickness, calculated from $\sqrt{3}/2 \times a_0 - D$ [74].

[f] Calculated by the Scherrer equation from XRD.

[g] Calculated from TEM.

Small-angle X-ray scattering (SAXS) experiments were performed for the support and Ni/Y catalysts. The corresponding patterns are shown in **Fig.3**. It can be seen that a primary reflection peak at 2θ of 0.89° and two small peaks at 2θ 1.44 and 1.62° are found for the SBA-16 material. These peaks are attributed to the reflections arising from the (110), (211), and (220) planes, respectively. The latter indicates that the presence of ordered mesopores with body-centered cubic symmetry (*Im3m*) [47,77]. The peak intensity of the (110) plane decreases slightly with increasing Y loading, which can be attributed to both effects of Ni and Y loading. As thermal pretreatment may cause a partial loss of the SBA-16 framework,

hence the calcination step can reduce the number of ordered mesopores [47,78]. Despite the occurrence of such a phenomenon, the TEM and SAXS confirm that the ordered mesoporous structure remained for all catalysts after Ni and Y introduction.

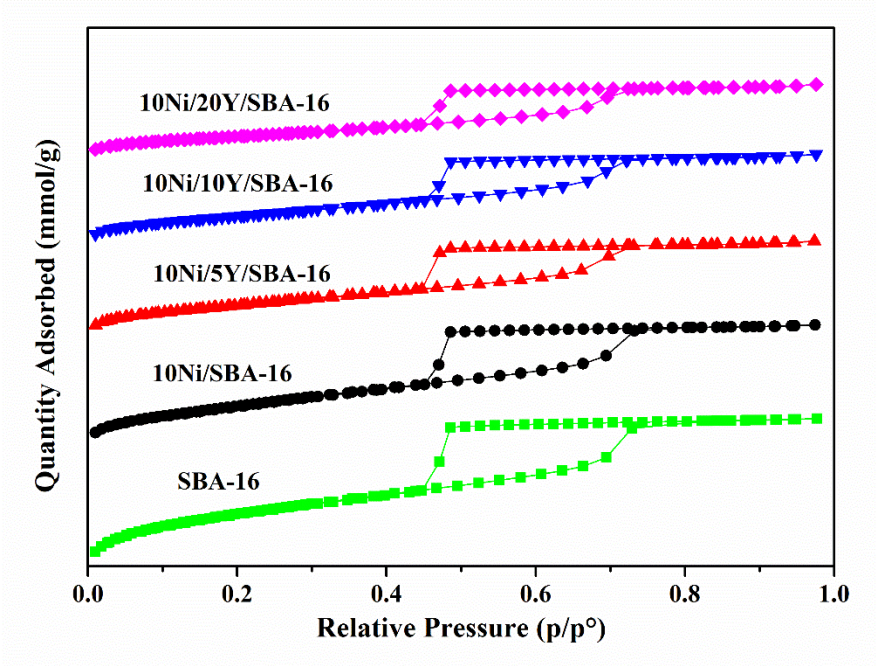

Figure. 2. N_2 adsorption-desorption isotherms of calcined SBA-16 support and Ni/xY/SBA-16 (x=0, 5, 10, and 20) catalysts with "x=0" referring to Ni/SBA-16.

It is worth noting that the structural parameters of the (110) plane of the support and catalysts were calculated from SAXS patterns. As shown in **Table 1**, parameters such as d_{110}, a_0, and H did not show significant changes when Ni and Y were introduced in SBA-16, indicating a remaining ordered structure of cage-like mesopores [71,77].

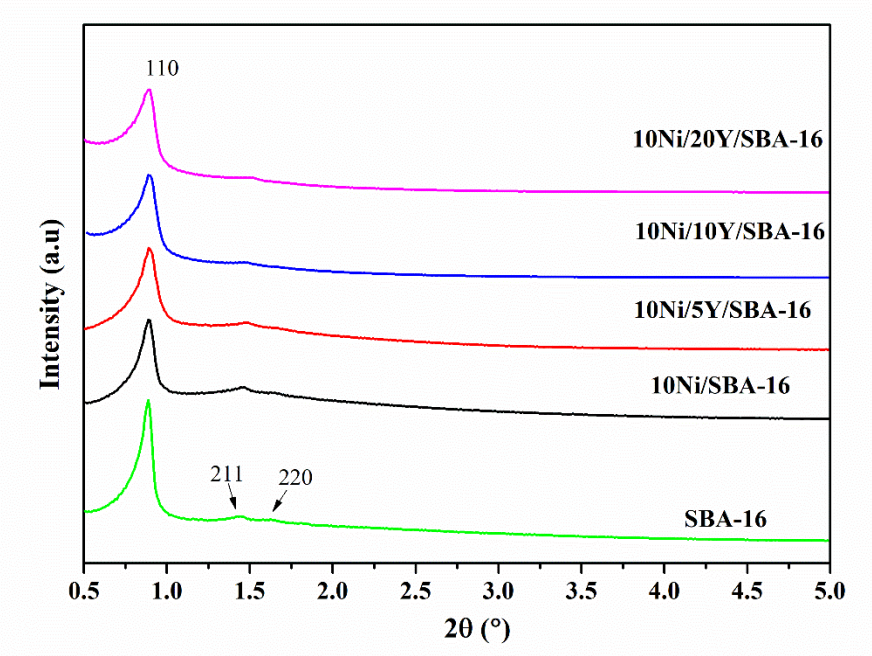

362

363 **Figure. 3.** SAXS patterns of calcined SBA-16 and Ni/xY/SBA-16 catalysts.

364

365 XRD patterns of the calcined and reduced catalysts are shown in **Fig.4**. The diffraction
366 peaks located at 2θ=37.2, 43.2, 62.8, 75.3, and 79.4° were assigned to the crystal planes of
367 (111), (200), (220), (311), and (222) (JCPDS-ICDD no. 78-0429) facet of face-centered
368 cubic crystalline NiO, respectively [79,80]. The broad peak located at 2θ= 22.9° was
369 attributed to the diffraction of the amorphous silica structure of SBA-16 [80]. No distinct
370 diffraction peaks were detected for yttrium-containing species. This suggests their high
371 dispersion over the SBA-16 matrix. The NiO diffraction peaks at 2θ=37.2, 43.2, and 62.8°
372 become sharper and more intensive with increasing content of Y. The crystalline size of
373 NiO was calculated and is presented in **Table 1**. The smallest NiO crystal size (4 nm) was
374 found on the Ni/SBA-16 catalyst. The NiO crystallite size increased up to 14-18 nm with
375 Y loading. This phenomenon can be linked with the decreased SSA and V_p with the
376 incorporation of Y, which leads to a decrease in the dispersion of Ni species.

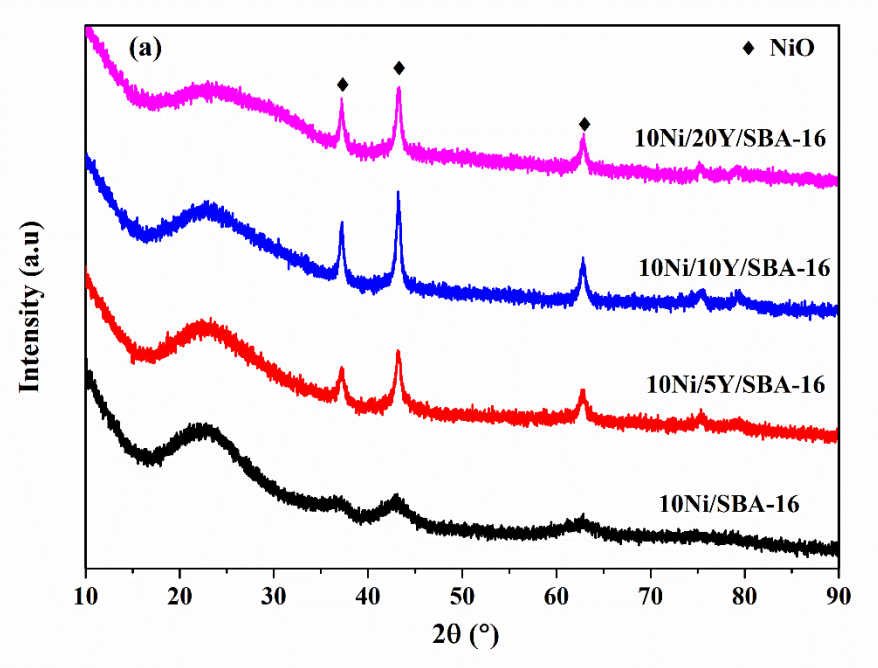

377

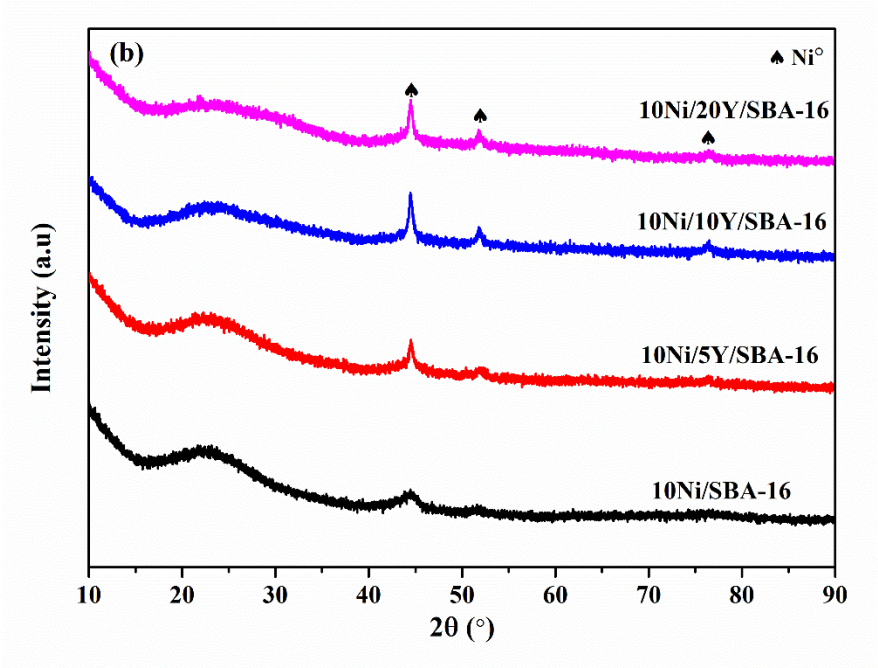

378

379 **Figure. 4.** XRD patterns of the calcined (a) and reduced (b) catalysts; Reduction condition: 500 °C for 1.5
380 h in 5%H_2/Ar; Flow rate: 100 mL/min.

381

XRD patterns of reduced catalysts are presented in **Fig.4b**. Thus, the diffraction peaks positioned at 2θ=44.5, 51.8, and 76.5˚ were attributed to the formation of metallic Ni. Still, after the reduction step, no diffraction peaks of yttrium species could be detected. The Ni^o crystalline size is presented in **Table 1**. The Ni^o crystalline size also increased with increasing Y loading.

To investigate the morphology of catalysts, TEM, HRTEM, and STEM-EDS mapping were carried out for the reduced catalysts. As shown in **Fig.5**, the TEM measurements confirmed the *Im3m* symmetry in all studied materials, indicating the preservation of an ordered mesoporous structure, which was consistent with the results of SAXS [77]. More micrographs displayed in **Fig.S2** showed a highly ordered structure of SBA-16.

It can be observed in **Fig.5** that more agglomerated Ni particles were detected on the high Y content catalysts. The particle size distribution graphs of Ni^o particles over the catalysts, obtained by the ImageJ software, are reported in **Fig.5**. With increasing the Y content, the highest frequency of Ni^o particle size shifted to a larger size. The mean particle size of Ni^o from TEM is reported in Table 1. One can note that the mean particle size of Ni^o increases significantly as the incorporation of Y with the larger particle size of Ni^o is found for 20 wt.% Y promoted catalyst.

400

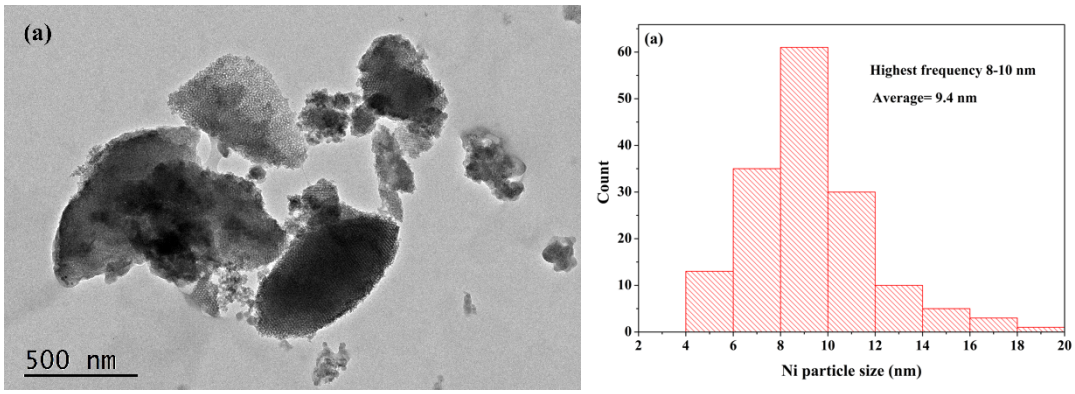

401

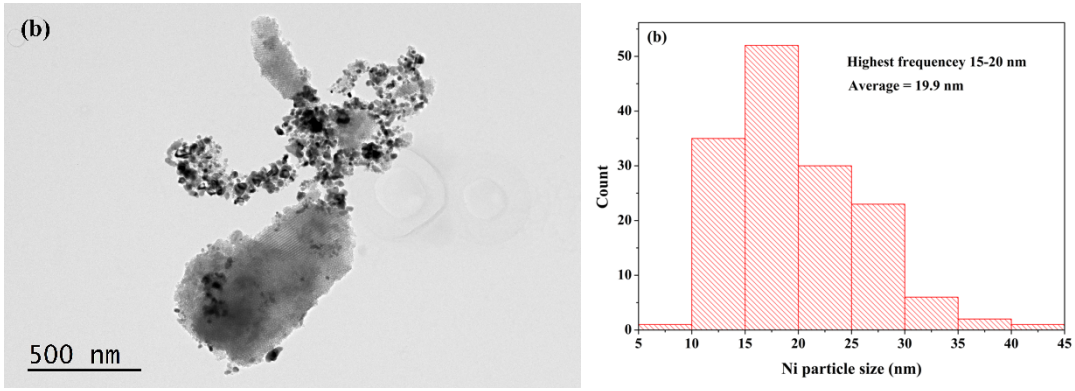

402

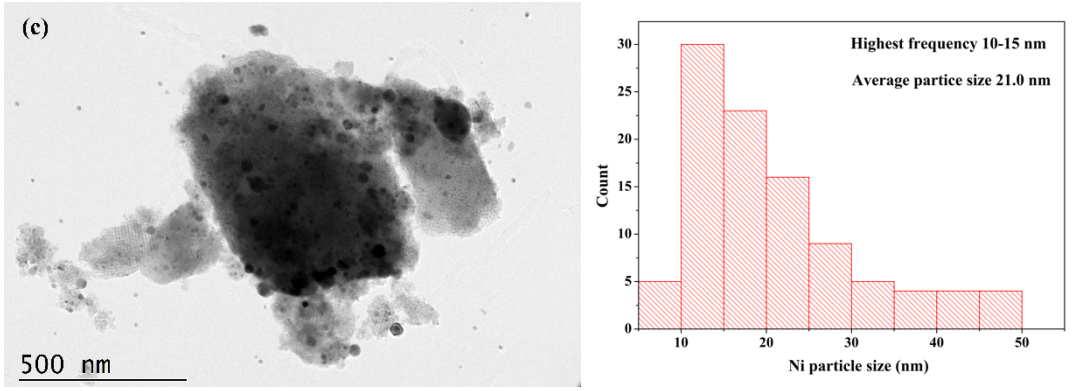

403

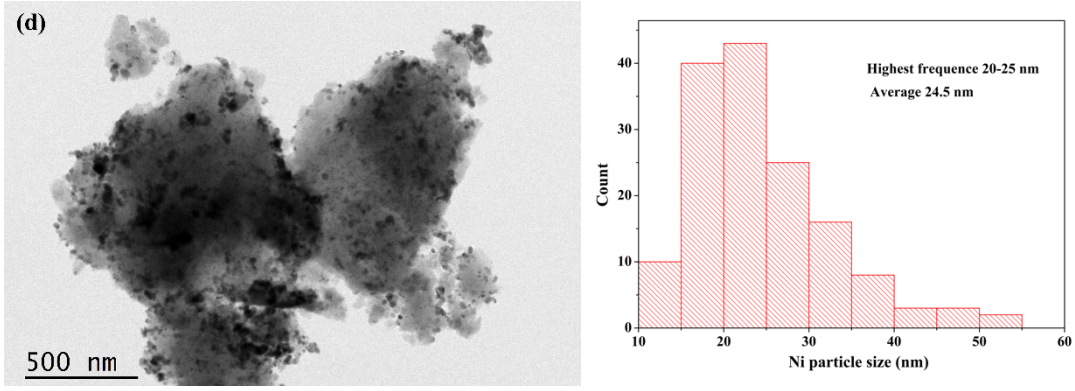

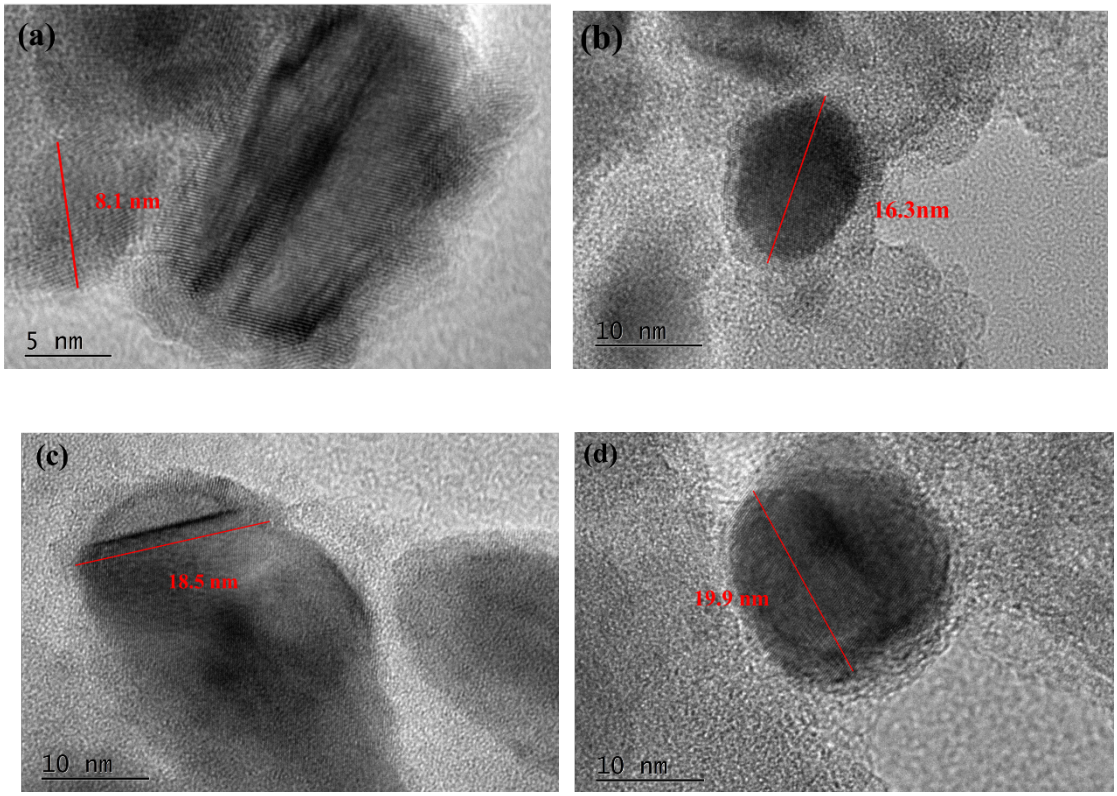

Figure. 5. TEM and HRTEM micrographs of reduced catalysts (500 °C for 1.5h) with the particle size distribution histogram; (a) 10Ni/SBA-16, (b) 10Ni/5Y/SBA-16, (c) 10Ni/10Y/SBA-16, (d) 10Ni/20Y/SBA-16.

The HRTEM measurements in **Fig.5** also confirm that Ni^{o} particle size increases with increasing of Y content. This could be explained by the decrease of the pore volume of support (Table 1) due to the deposition of Y species inside mesopores of SBA-16. The same phenomenon was also found on ceria-doped Ni/SBA-16 catalysts [29].

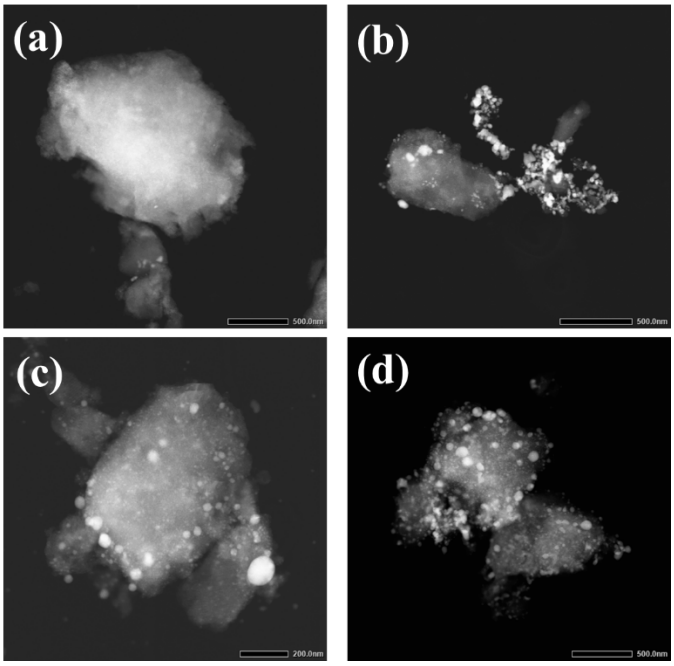

416

417

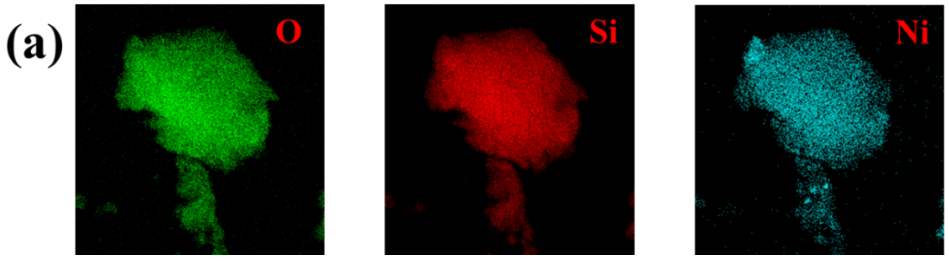

418

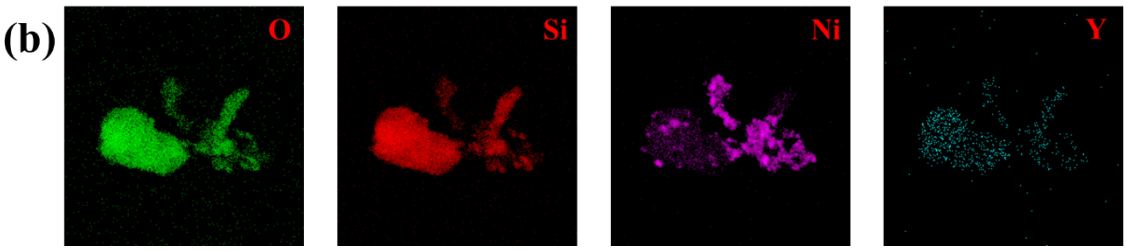

419

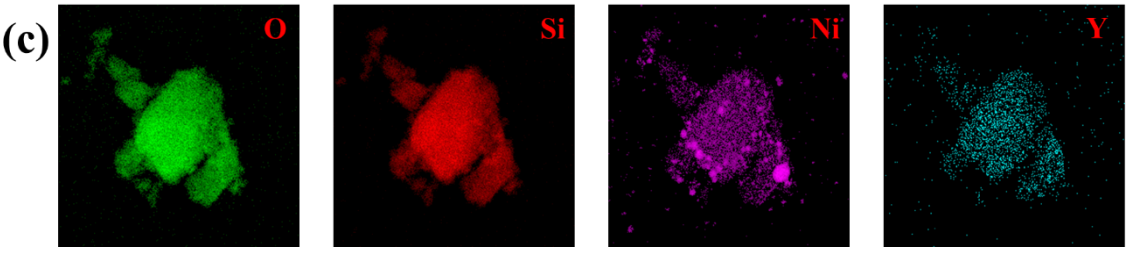

420

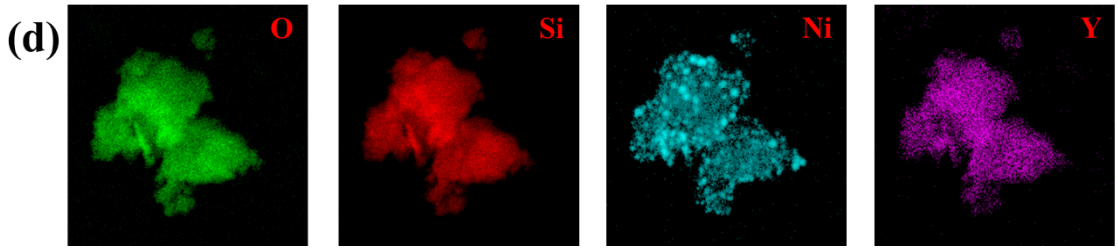

Figure. 6. STEM-EDS elemental mapping images of reduced catalysts; (a) 10Ni/SBA-16, (b) 10Ni/5Y/SBA-16, (c) 10Ni/10Y/SBA-16, (d) 10Ni/20Y/SBA-16.

STEM-EDS mapping was also performed to investigate the elemental distribution of Ni and Y. As shown in **Fig.6**, the Ni species were evenly dispersed on the surface of Ni/SBA-16. This accounts for the small particle size obtained by XRD and TEM. As for Ni/Y/SBA-16 catalysts, Y species were highly dispersed over the support which is in good agreement with the XRD results. Still, in the studied catalysts the increasing Y loading led to the formation of Ni particles with a bigger diameter than those observed in Ni/SBA-15. Nevertheless, their presence did not negatively affect the catalytic performance. Indeed, the yttrium-promoted samples were more active and selective in the studied reaction.

To investigate the surface composition of the catalysts, XPS experiments were carried out on the reduced catalysts. The corresponding XPS spectra are displayed in **Fig. S3**.

In **Fig.S3a**, it can be seen from the Ni2p spectra that the peak intensity of Ni2p increased with the increasing loading of Y. This can be explained by the agglomeration of Ni particles as shown by XRD, TEM, and STEM-EDS. The peaks at 853.3 and 856.1 eV were attributed to Ni^{o} and Ni^{2+} species, respectively. The presence of Ni^{2+} species could be attributed to the exposure to air before XPS analysis. The ratio of Ni^{o}/Ni^{2+} increases with the Y loading. In **Table 2**, the Ni/Si ratio increase with the incorporation of Y, indicating more Ni species

on the surface of the support which is in good agreement with the results obtained by TEM. The binding energy of $Ni2p_{3/2}$ follows a decreasing trend with Y addition, indicating an increase of Ni-support interaction [65].

In **Fig. S3b**, the XPS O1s spectra of catalysts are presented. The peak located at 532.9 eV was assigned to the lattice oxygen (O_L) of SiO_2 [65,81]. The binding energy of O1s of Y-doped catalysts shifted to a lower position as compared to the Y-free sample, indicating the formation of a Si-O-Y chemical bond [82]. After modification with Y, the peak appeared at around 531.0 eV and was attributed to lattice oxygen (O_M) of Y_2O_3 [65,83]. By increasing Y content, the peak intensity of O_L decreased with the increase of peak intensity of O_M. The peak positioned at 534.0 eV was attributed to the presence of adsorbed oxygen species such as hydroxyl species (O_{OH}) [84,85]. The content of O_{OH}/ (O_{OH}+ O_L+ O_M) of catalysts was shown in **Table 2**. It can be seen that the O_{OH} ratio increased with the increasing loading of Y.

The Si2p spectra of catalysts are shown in **Fig.S3c**. The peak intensity of Si2p located at 103.7 eV decreased due to the deposition of metals on the surface of the support. The binding energy of Si2p of Y-doped catalysts also showed a shift towards a lower position compared to Y-free catalysts suggesting the formation of Si-O-Y chemical bond [82].

In **Fig.S3d**, the peaks located at 158.3 and 160.4 eV were assigned to $Y3d_{5/2}$ and $Y3d_{3/2}$, respectively [65,86]. As for the peak positioned at 154.7, it was attributed to the spectrum of Si2s [65]. With increasing yttrium content, the peak intensity of Y3d increases with the weakening of Si2p and Si2s (**Fig. S3c** and **d**), indicating more Y-species on the surface. In **Table 2**, one can see that the Y/Si ratio increased with the increasing loading of Y, indicating more Y species on the surface of the support. The binding energy of $Y3d_{5/2}$ of

Y-doped catalysts has witnessed a small increase from 158.0 to 158.3 eV, implying increased Y-Si interaction.

Table 2 Surface composition and binding energies of the reduced catalysts from XPS.

Catalyst	Atomic ratio (%)				Binding Energy (eV)	
	Ni/Si	Y/Si	$O_{OH}/ (O_{OH}+ O_L+ O_M)$	Ni^0/Ni^{2+}	$Ni2p_{3/2}$	$Y3d_{5/2}$
10Ni/SBA-16	1.6	ND	3.8	23.5	856.1	ND
10Ni/5Y/SBA-16	7.5	18.6	14.3	40.5	855.4	158.0
10Ni/10Y/SBA-16	16.0	23.1	17.2	60.0	855.3	158.1
10Ni/20Y/SBA-16	13.3	25.8	15.8	41.3	855.4	158.3

3.3 On the reducibility of the catalysts from H_2-TPR

The reducibility of catalysts was studied by H_2-TPR. The reduction profiles are presented in **Fig.7**. The registered maximum temperature of reduction and H_2 uptake are listed in **Table S1**. The reduction peaks were calibrated by pure CuO. It has been reported that the reduction of Y_2O_3 is very difficult with only a slight reduction peak located at around 650 ℃, which only accounts for 0.24% of the total reduction of the Y_2O_3 oxide [87]. Thus, it can be assumed that the reduction of Y is negligible and the reduction peaks of catalysts can be mostly attributed to the reduction of nickel species [65].

The reduction peaks of Ni/SBA-16 consisted of mainly two broad peaks with maxima located at 485 (γ) and 642℃ (δ), respectively. These two peaks were attributed to the reduction of nickel species located outside as well as inside the pores of SBA-16 as reported

480 elsewhere [88]. Higher reduction temperature is needed to reduce nickel particles placed
481 inside the 3-dimensional pore network. As confirmed by XRD and TEM, the particles of
482 Ni were particularly small for Ni/SBA-16 which explains the reducibility profile shifted
483 towards higher temperatures. This observation agrees well with XPS, suggesting that most
484 Ni species were inside the mesopores.

485 For Ni/xY/SBA-16 catalysts, the weak α peak located at around 250℃ was attributed to
486 the reduction of NiO with weak or no interaction with the support [89,90]. The sharp peak
487 β at 370-400℃ and the shoulder peak γ at around 450℃ were assigned to the reduction of
488 NiO with weak or medium interaction with the support [47,89]. The broad peak δ with the
489 maximum at around 650℃ can be attributed to the reduction of NiO species either located
490 inside the pores of SBA-16 or well-dispersed over the support. The latter may be linked
491 with the formation of nickel hydrosilicate species [47,91]. The Ni/xY/SBA-16 catalysts
492 presented more NiO species being able to reduce at lower temperatures (β and γ), compared
493 to those reported for Ni/SBA-16 (**Fig.7** and **Table S1**). This can be attributed to the
494 formation of bulk NiO species as already shown by XRD and TEM.

495

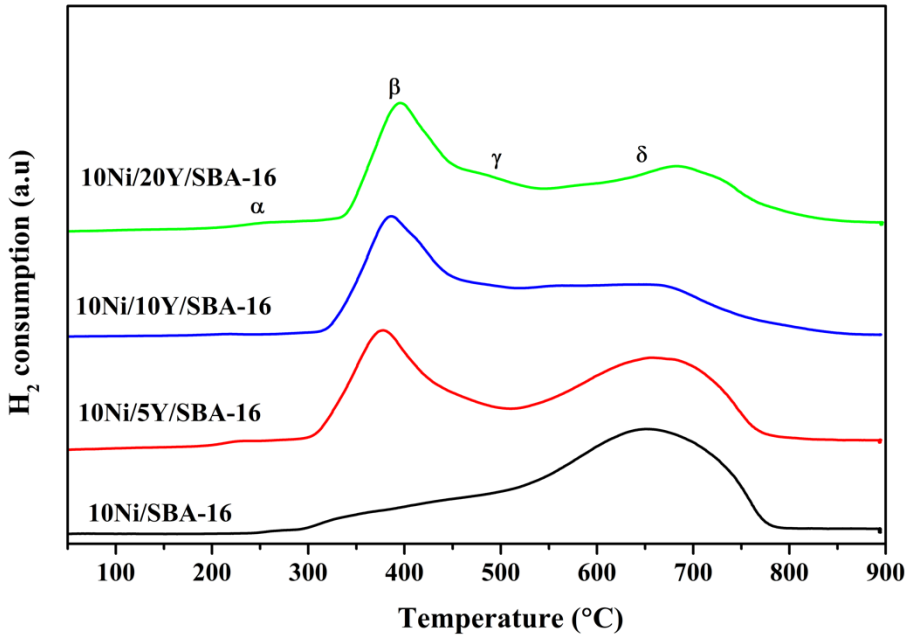

496

497 **Figure. 7.** H_2-TPR profiles of (a) 10Ni/SBA-16, (b) 10Ni/5Y/SBA-16, (c) 10Ni/10Y/SBA-16, and (d)
498 10Ni/20Y/SBA-16.

499

500 **3.4 On the basicity of the catalysts from CO_2-TPD**

501 To investigate the surface basicity of the reduced catalysts, the CO_2-TPD experiments were
502 carried out. The profiles are displayed in **Fig.8**. It has been reported that the CO_2 desorption
503 peak located at 100-220℃ was attributed to the weak basic sites, which were related to the
504 bicarbonate species due to the interaction between hydroxyl species on the silica and
505 adsorbed CO_2 molecules [9,92,93]. The desorption peaks positioned between 200 and 400℃
506 were assigned to the moderate basic sites, which were related to metal-oxygen pairs
507 [9,93,94]. The basicity distribution of catalysts is shown in **Table 3**. It is important to note
508 that Y addition led to a decrease of weak sites with an increase of medium basic sites and
509 with a corresponding decrease of weak basic sites. The highest number of medium basic
510 sites was obtained over 10 wt.% Y-doped sample. Also, the CO_2 desorption peak

corresponding to weak basic sites shifted from 150℃ for Ni/SBA-16 to 95℃ for Ni/Y/SBA-16. As the methanation reaction was tested between 200 and 450℃, the weak basic sites of Ni/Y/SBA-16 catalysts may have slight effects on the performance of catalysts. There are no desorption peaks at a temperature higher than 500℃, relating to the strong basic sites, which might be caused by low-coordination surface oxygen atoms [93]. In XPS analysis, it was found that doping Y promotes the formation of Si-O-Y chemical bonds, which may account for the increased moderate basic sites [93]. Furthermore, it has been demonstrated that the strong basic sites did not participate in the CO_2 methanation process [9]. Meanwhile, the moderate basic sites play a significant role in the CO_2 methanation reaction [95]. Thus, it can be speculated that the reported increase of medium basic sites in Ni/Y/SBA-16 catalysts favored catalytic performance in the studied reaction.

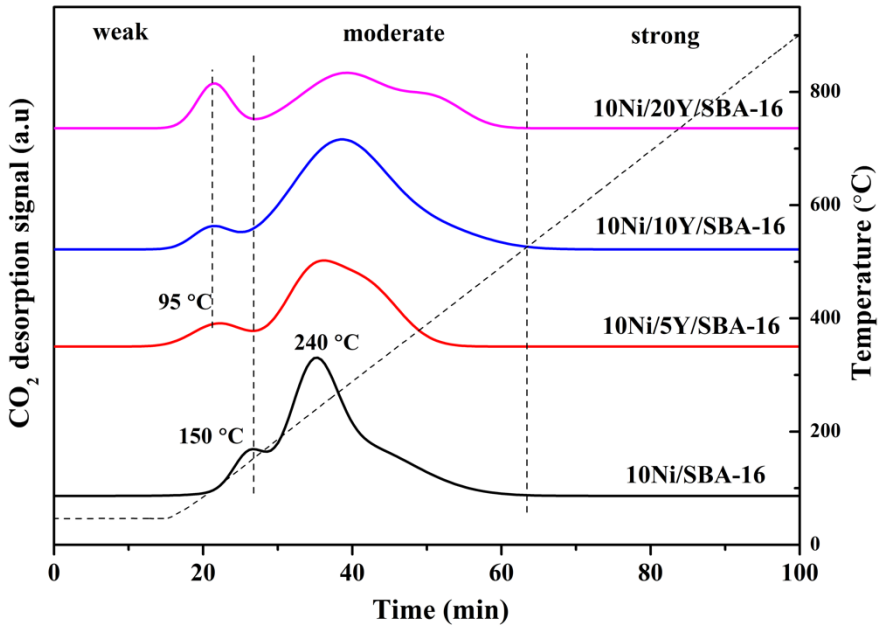

Figure. 8. CO_2 desorption profiles for the reduced (a) 10Ni/SBA-16, (b) 10Ni/5Y/SBA-16, (c) 10Ni/10Y/SBA-16, and (d) 10Ni/20Y/SBA-16.

Table 3 Basic site distribution of the catalysts from CO_2-TPD.

Catalyst	Basic sites [μmol/g_{cat}]		Total basic sites [μmol/g_{cat}]	Distribution of basic sites [%]	
	weak	moderate		weak	moderate
10Ni/SBA-16	28.9	34.3	63.2	45.7	54.3
10Ni/5Y/SBA-16	6.6	41.6	48.2	13.7	86.3
10Ni/10Y/SBA-16	4.3	65.5	69.8	6.2	93.8
10Ni/20Y/SBA-16	10.0	43.0	53.0	18.9	81.1

3.5 Correlation between the catalytic performance and physicochemical properties of the studied catalysts

To draw a correlation between the physicochemical properties and the activity of catalysts, the CO_2 reaction rate (**Table 4**) was calculated for all the catalysts and correlated to parameters such as Ni^o particle size (TEM), surface Ni^o molar ratio (XPS), moderate basic sites (CO_2-TPD), and surface Ni/Si molar ratio (XPS). The corresponding features are shown in **Fig.9**. One can note that the surface parameters such as basicity, Ni^o particle size, Ni/Si molar ratio, etc. of the catalysts increase with the Y loading until 10 wt.%, indicating that the addition of Y significantly modified the structural and chemical properties of the catalysts. The promotion with Y leads to agglomeration of Ni particles on the support and more Ni species on the surface of the support due to deposition of Y over the SBA-16 matrix. Meanwhile, the moderate basicity of catalysts also shows an increasing trend as the increase of Y loading until 10wt.% d.

The reaction rate of CO_2 at 350 ^oC and the TOF of CO_2 at 300 ^oC were calculated (**Table 4)**. It is worth noting that the CO_2 reaction rate increases with the increasing Y loading

543 until an optimal content of 10 wt.%. When the Y content increased up to 20 wt.%, the SSA
544 and V_p of Ni/Y/SBA-16 catalyst then decreased (**Table 1**, 343 m^2/g, 0.39 cm^3/g).
545 Furthermore, on such catalysts, an agglomeration of Ni particles was detected by TEM,
546 and the mean particle size of Ni° reached 24.5 nm with a high distribution frequency of
547 particle sizes at 20-25 nm. The $O_{OH}/ (O_{OH}+ O_L+ O_M)$ ratio and moderate basic sites also
548 decrease over the 20 wt.% Y-doped catalyst. Thus, the CO_2 reaction rate decreased. A good
549 correlation between CO_2 reaction rate and moderate basic sites can be drawn as presented
550 in **Fig. 10**. One can note that a linear correlation between r_{CO2} and the number of moderate
551 basic sites can be established. In the study of Pan et al., it has been demonstrated that
552 moderate basicity played an important role as they can promote the formation of
553 monodentate carbonates, enhancing activity in CO_2 methanation [95].

554

555 **Table 4.** CO_2 reaction rate at 350°C of catalysts and TOF at 300°C.

Catalyst	CO_2 reaction rate at 350°C ($mmol/g_{cat}\cdot min$)	TOF at 300°C (s^{-1})
10Ni/SBA-16	1.68	0.04
10Ni/5Y/SBA-16	1.90	0.09
10Ni/10Y/SBA-16	2.84	0.27
10Ni/20Y/SBA-16	1.86	0.18

556

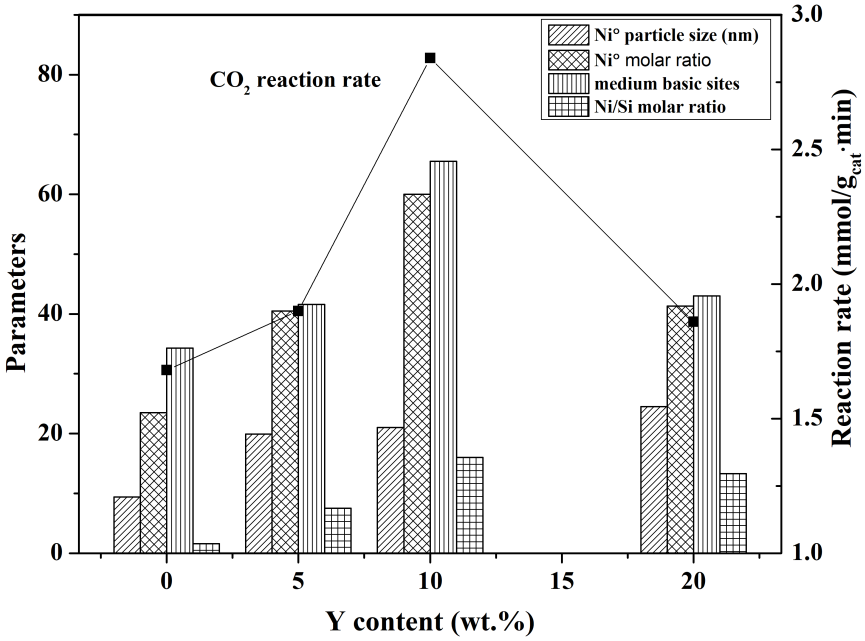

Figure. 9. Correlating graphs between the parameters Ni^{o} particle size (TEM), surface Ni^{o} molar ratio (XPS), medium basic sites (CO_2-TPD), and surface Ni/Si molar ratio (XPS) and CO_2 reaction rate at 350°C; The 0 wt.% of Y corresponding to 10Ni/SBA-16.

The TOF values, calculated at 300°C for CO_2 methanation, are presented in **Table 4**. As for the rates, the TOF values can be easily correlated with the moderate basic sites as shown in **Fig.10**. A linear correlation between the number of moderate basic sites and the TOF values has been reported, except for the catalyst with 20 wt.% of Y. This correlation confirms that a large number of moderate basic sites on the surface of the catalyst can favor the adsorption and reaction of CO_2. It was reported by other authors that the TOF values had a good correlation with the total basicity of Ni-Mg/SBA-15 catalysts with different content of Mg [9]. In the present study, we demonstrated the crucial role of moderate basic sites of Ni/Y/SBA-16 catalysts in CO_2 methanation reaction.

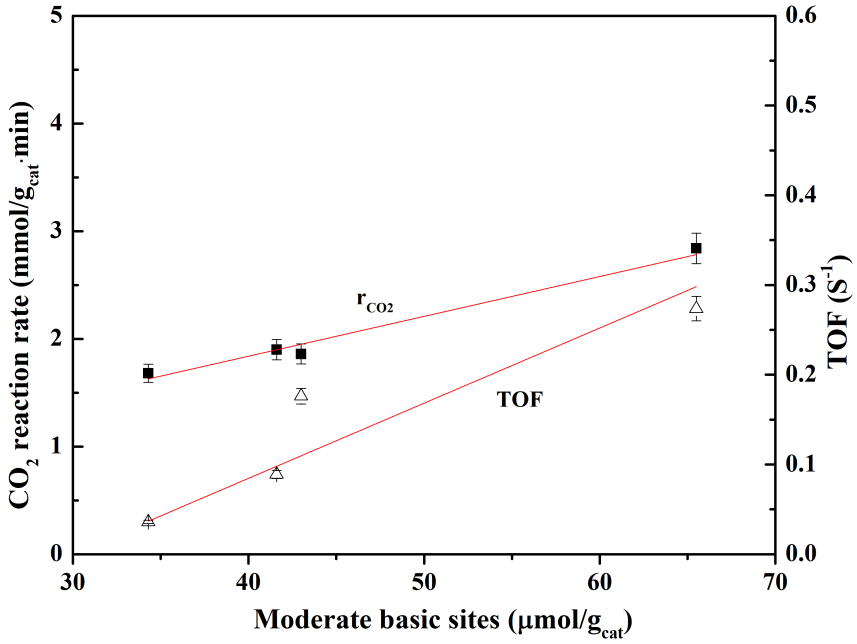

572

573 **Figure. 10.** Linear correlation between TOF (300°C) and CO_2 reaction rate with moderate basic sites (error
574 bar of 5%).

575

576 **3.6 Stability tests of Ni/xY/SBA-16 catalysts in CO_2 methanation**

577 To study the stability of the studied catalysts in time on stream, a catalytic test has been
578 carried out at 350 °C for 8 h. The CO_2 conversion and CH_4 selectivity of catalysts during
579 time-on-stream (TOS) are presented in **Fig.11**. The green lines in **Fig.11** represent the
580 equilibrium line of CO_2 conversion and CH_4 selectivity, respectively. It can be seen from
581 **Fig.11** that both the CO_2 conversion and CH_4 selectivity showed high stability during the
582 TOS test. with 10Ni/10Y/SBA-16 catalyst presenting the best catalytic performance. It is
583 worth noting that no activity loss, linked with a possible deactivation of the catalysts, was
584 observed.

585

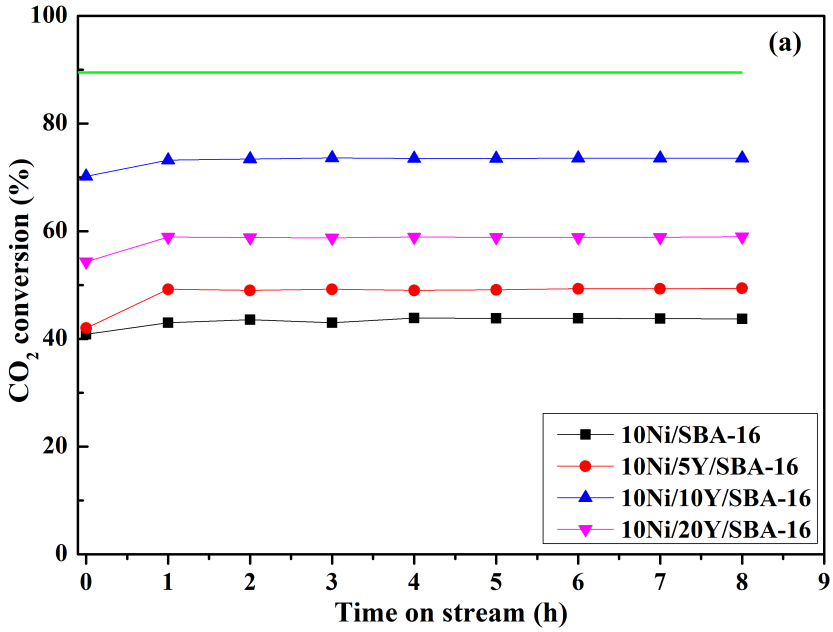

586

587

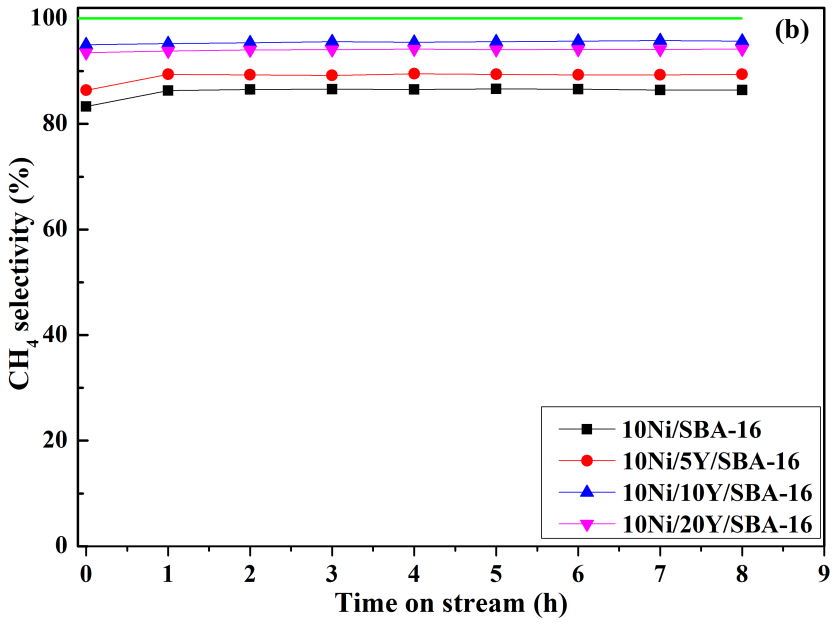

588

589 **Figure. 11.** CO_2 methanation performance at 350 °C in terms of (a) CO_2 conversion and (b) CH_4 selectivity
590 with time on stream (TOS) over 10Ni/SBA-16 and 10Ni/xY/SBA-16 catalysts.

591

3.7 Characterization of catalysts after test

The XRD patterns of the catalysts after the methanation test (shown **2.3**) are shown in **Fig.S4**, revealing only the diffraction peaks of metallic Ni after the test. Only a broad peak of Ni^0 was found for the 10Ni/SBA-16 catalyst, indicating that a high dispersion was kept after the test. The crystalline size of Ni metal for Y-promoted catalysts was calculated and listed in **Table S2**. One can note that no significant differences in Ni crystalline sizes were observed for the reduced and spent catalysts, except for 10Ni/20Y/SBA-16 which size significantly increased. This suggests for the latter sample possible sintering of Ni° particles. However, during the stability test, all studied samples showed highly stable CO_2 conversion and CH_4 selectivity. In this regard, this possible sintering was not significant to affect the activity during the initial 8h test.

Furthermore, to determine possible carbon deposition over the catalysts, the TGA/DSC-MS measurements were performed after methanation. The profiles are presented in **Fig.S5**. All studied materials showed a sharp mass loss from the starting temperature to 100°C, which was caused by the removal of adsorbed water as determined by the MS signal (m/z=18). A peak of CO_2 was detected by MS (m/z=44) in the range of 200-400°C for all the spent catalysts, which was assigned to possible traces of carbonaceous species [31,96]. The slight increase of weight at 350-450°C for Y-promoted catalysts was attributed to the oxidization of metallic Ni [97]. Finally, DSC curves did not show significant peaks corresponding to the removal of bulk carbon, confirming only traces of a possible carbon deposition [98].

4. Conclusions

An ordered mesoporous silica SBA-16 with high specific surface area (SSA) and pore volume (V_p) was synthesized. The Ni/Y/SBA-16 catalysts with different loading of Y were prepared by sequential impregnation. The CO_2 methanation activity tests showed that modification with Y promoted the CO_2 conversion and CH_4 selectivity with 10 wt.% Y-doped catalyst showing the best performance.

The promotion of the studied catalysts by yttrium led to a decrease of SSA and V_p accompanied by the increase of Ni particle size. Also, the adsorbed surface oxygen species increased with the yttrium loading. Furthermore, it was found that the number of moderate basic sites increased with the loading of Y with a maximum of 10 wt.%Y (10Ni/10Y/SBA-16). Finally, the CO_2 reaction rate and turnover frequency of CO_2 conversion were well correlated to the number of moderate basic sites. And, no sintering of nickel species and formation of carbon after CO_2 methanation were observed even after an 8h run.

Acknowledgments

Chao Sun wants to thank the China Scholarship Council (CSC) for the fund for the Ph.D. studying at Sorbonne Université. Katarzyna Świrk is an MSCA-IF-funded researcher at the Norwegian University of Science and Technology in Norway. This project has received funding from the European Union's Horizon 2020 research and innovation program under the Marie Skłodowska-Curie grant agreement No 892571.

References

[1] Martínez-Zarzoso I, Maruotti A. The impact of urbanization on CO2 emissions: Evidence from developing countries. Ecol Econ 2011;70:1344–53. https://doi.org/10.1016/j.ecolecon.2011.02.009.

[2] Yu KMK, Curcic I, Gabriel J, Tsang SCE. Recent advances in CO2 capture and utilization. ChemSusChem 2008;1:893–9. https://doi.org/10.1002/cssc.200800169.

[3] Götz M, Lefebvre J, Mörs F, McDaniel Koch A, Graf F, Bajohr S, et al. Renewable Power-to-Gas: A technological and economic review. Renew Energy 2016;85:1371–90. https://doi.org/10.1016/j.renene.2015.07.066.

[4] Schaaf T, Grünig J, Schuster MR, Rothenfluh T, Orth A. Methanation of CO2 - storage of renewable energy in a gas distribution system. Energy Sustain Soc 2014;4:1–14. https://doi.org/10.1186/s13705-014-0029-1.

[5] Mikhail M, Da Costa P, Amouroux J, Cavadias S, Tatoulian M, Ognier S, et al. Electrocatalytic behaviour of CeZrOx-supported Ni catalysts in plasma assisted CO2 methanation. Catal Sci Technol 2020;10:4532–43. https://doi.org/10.1039/d0cy00312c.

[6] Sabatier P. Nouvelles synthèses du méthane. Comptes Rendus Acad Sci 1902;82:514–6.

[7] Aresta M, Dibenedetto A, Angelini A. Catalysis for the valorization of exhaust carbon: From CO2 to chemicals, materials, and fuels. technological use of CO2. Chem Rev 2014;114:1709–42. https://doi.org/10.1021/cr4002758.

[8] Peter SC. Reduction of CO2 to Chemicals and Fuels: A Solution to Global Warming and Energy Crisis. ACS Energy Lett 2018;3:1557–61. https://doi.org/10.1021/acsenergylett.8b00878.

[9] Hongmanorom P, Ashok J, Zhang G, Bian Z, Wai MH, Zeng Y, et al. Enhanced performance and selectivity of CO2 methanation over phyllosilicate structure derived Ni-Mg/SBA-15 catalysts. Appl Catal B Environ 2021;282:119564. https://doi.org/10.1016/j.apcatb.2020.119564.

[10] Karelovic A, Ruiz P. CO2 hydrogenation at low temperature over Rh/γ-Al2O3 catalysts: Effect of the metal particle size on catalytic performances and reaction mechanism. Appl Catal B Environ 2012;113–114:237–49. https://doi.org/10.1016/j.apcatb.2011.11.043.

[11] Athanasia Petalaa, Paraskevi Panagiotopoulou. Methanation of CO2 over alkali-promoted Ru/TiO2 catalysts: I. Effect of alkali additives on catalytic activity and selectivity. Appl Catal B Environ 2018;224:919–27. https://doi.org/10.1016/j.apcatb.2018.06.055.

[12] Kim HY, Lee HM, Park J. Bifunctional Mechanism of CO2 Methanation on Pd-MgO/SiO2 Catalyst: Independent Roles of MgO and Pd on CO2 Methanation. J Phys Chem C 2010;114:7128–31.

[13] Sun C, Beaunier P, La Parola V, F. Liotta L, Da Costa P. Ni/CeO2 Nanoparticles Promoted by Yttrium Doping as Catalysts for CO2 Methanation. ACS Appl Nano Mater 2020;3:12355–68. https://doi.org/10.1021/acsanm.0c02841.

[14] Zhou G, Wu T, Xie H, Zheng X. Effects of structure on the carbon dioxide

methanation performance of Co-based catalysts. Int J Hydrogen Energy 2013;38:10012–8. https://doi.org/10.1016/j.ijhydene.2013.05.130.

[15] Jacquemin M, Beuls A, Ruiz P. Catalytic production of methane from CO2 and H2 at low temperature: Insight on the reaction mechanism. Catal Today 2010;157:462–6. https://doi.org/10.1016/j.cattod.2010.06.016.

[16] Wang F, He S, Chen H, Wang B, Zheng L, Wei M, et al. Active Site Dependent Reaction Mechanism over Ru/CeO2 Catalyst toward CO2 Methanation. J Am Chem Soc 2016;138:6298–305. https://doi.org/10.1021/jacs.6b02762.

[17] Aziz MAA, Jalil AA, Triwahyono S, Ahmad A. CO2 methanation over heterogeneous catalysts: Recent progress and future prospects. Green Chem 2015;17:2647–63. https://doi.org/10.1039/c5gc00119f.

[18] Tada S, Shimizu T, Kameyama H, Haneda T, Kikuchi R. Ni/CeO2 catalysts with high CO2 methanation activity and high CH4 selectivity at low temperatures. Int J Hydrogen Energy 2012;37:5527–31. https://doi.org/10.1016/j.ijhydene.2011.12.122.

[19] Zhu M, Tian P, Cao X, Chen J, Pu T, Shi B, et al. Vacancy engineering of the nickel-based catalysts for enhanced CO2 methanation. Appl Catal B Environ 2021;282:119561. https://doi.org/10.1016/j.apcatb.2020.119561.

[20] Rui N, Zhang X, Zhang F, Liu Z, Cao X, Xie Z, et al. Highly active Ni/CeO2 catalyst for CO2 methanation: Preparation and characterization. Appl Catal B Environ 2021;282:119581. https://doi.org/10.1016/j.apcatb.2020.119581.

[21] Guilera J, Del Valle J, Alarcón A, Díaz JA, Andreu T. Metal-oxide promoted Ni/Al2O3 as CO2 methanation micro-size catalysts. J CO2 Util 2019;30:11–7. https://doi.org/10.1016/j.jcou.2019.01.003.

[22] Zhang J, Xin Z, Meng X, Lv Y, Tao M. Effect of MoO3 on structures and properties of Ni-SiO2 methanation catalysts prepared by the hydrothermal synthesis method. Ind Eng Chem Res 2013;52:14533–44. https://doi.org/10.1021/ie401708h.

[23] Wang K, Men Y, Liu S, Wang J, Li Y, Tang Y, et al. Decoupling the size and support/metal loadings effect of Ni/SiO2 catalysts for CO2 methanation. Fuel 2021;304:121388. https://doi.org/10.1016/j.fuel.2021.121388.

[24] Ye RP, Liao L, Reina TR, Liu J, Chevella D, Jin Y, et al. Engineering Ni/SiO2 catalysts for enhanced CO2 methanation. Fuel 2021;285:119151. https://doi.org/10.1016/j.fuel.2020.119151.

[25] Jia X, Zhang X, Rui N, Hu X, Liu C jun. Structural effect of Ni/ZrO2 catalyst on CO2 methanation with enhanced activity. Appl Catal B Environ 2019;244:159–69. https://doi.org/10.1016/j.apcatb.2018.11.024.

[26] Ashok J, Ang ML, Kawi S. Enhanced activity of CO2 methanation over Ni/CeO2-ZrO2 catalysts: Influence of preparation methods. Catal Today 2017;281:304–11. https://doi.org/10.1016/j.cattod.2016.07.020.

[27] Zhou R, Rui N, Fan Z, Liu C jun. Effect of the structure of Ni/TiO2 catalyst on CO2 methanation. Int J Hydrogen Energy 2016;41:22017–25. https://doi.org/10.1016/j.ijhydene.2016.08.093.

721 [28] Liu D, Quek XY, Cheo WNE, Lau R, Borgna A, Yang Y. MCM-41 supported
722 nickel-based bimetallic catalysts with superior stability during carbon dioxide
723 reforming of methane: Effect of strong metal-support interaction. J Catal
724 2009;266:380–90. https://doi.org/10.1016/j.jcat.2009.07.004.

725 [29] Sun C, Beaunier P, Da Costa P. Effect of ceria promotion on the catalytic
726 performance of Ni/SBA-16 catalysts for CO2 methanation. Catal Sci Technol
727 2020;10:6330–41. https://doi.org/10.1039/d0cy00922a.

728 [30] González-Castaño M, de Miguel JCN, Penkova A, Centeno MA, Odriozola JA,
729 Arellano-Garcia H. Ni/YMnO3 perovskite catalyst for CO2 methanation. Appl
730 Mater Today 2021;23:27–30. https://doi.org/10.1016/j.apmt.2021.101055.

731 [31] Sun C, Świrk K, Wierzbicki D, Motak M, Grzybek T, Da Costa P. On the effect of
732 yttrium promotion on Ni-layered double hydroxides-derived catalysts for
733 hydrogenation of CO2 to methane. Int J Hydrogen Energy 2021;46:12169–79.
734 https://doi.org/10.1016/j.ijhydene.2020.03.202.

735 [32] Wierzbicki D, Debek R, Motak M, Grzybek T, Gálvez ME, Da Costa P. Novel Ni-
736 La-hydrotalcite derived catalysts for CO2 methanation. Catal Commun 2016;83:5–
737 8. https://doi.org/10.1016/j.catcom.2016.04.021.

738 [33] Wierzbicki D, Baran R, Dębek R, Motak M, Gálvez ME, Grzybek T, et al.
739 Examination of the influence of La promotion on Ni state in hydrotalcite-derived
740 catalysts under CO2 methanation reaction conditions: Operando X-ray absorption
741 and emission spectroscopy investigation. Appl Catal B Environ 2018;232:409–19.
742 https://doi.org/10.1016/j.apcatb.2018.03.089.

743 [34] Wierzbicki D, Motak M, Grzybek T, Gálvez ME, Da Costa P. The influence of
744 lanthanum incorporation method on the performance of nickel-containing
745 hydrotalcite-derived catalysts in CO2 methanation reaction. Catal Today
746 2018;307:205–11. https://doi.org/10.1016/j.cattod.2017.04.020.

747 [35] Wierzbicki D, Moreno MV, Ognier S, Motak M, Grzybek T, Da Costa P, et al. Ni-
748 Fe layered double hydroxide derived catalysts for non-plasma and DBD plasma-
749 assisted CO2 methanation. Int J Hydrogen Energy 2020;45:10423–32.
750 https://doi.org/10.1016/j.ijhydene.2019.06.095.

751 [36] Wierzbicki D, Baran R, Dębek R, Motak M, Grzybek T, Gálvez ME, et al. The
752 influence of nickel content on the performance of hydrotalcite-derived catalysts in
753 CO2 methanation reaction. Int J Hydrogen Energy 2017;42:23548–55.
754 https://doi.org/10.1016/j.ijhydene.2017.02.148.

755 [37] Le TA, Kim MS, Lee SH, Kim TW, Park ED. CO and CO2 methanation over
756 supported Ni catalysts. Catal Today 2017;293–294:89–96.
757 https://doi.org/10.1016/j.cattod.2016.12.036.

758 [38] Aziz MAA, Jalil AA, Triwahyono S, Mukti RR, Taufiq-Yap YH, Sazegar MR.
759 Highly active Ni-promoted mesostructured silica nanoparticles for CO2
760 methanation. Appl Catal B Environ 2014;147:359–68.
761 https://doi.org/10.1016/j.apcatb.2013.09.015.

762 [39] Italiano C, Llorca J, Pino L, Ferraro M, Antonucci V, Vita A. CO and CO2
763 methanation over Ni catalysts supported on CeO2, Al2O3 and Y2O3 oxides. Appl
764 Catal B Environ 2020;264:118494. https://doi.org/10.1016/j.apcatb.2019.118494.

765 [40] Shanmugam V, Neuberg S, Zapf R, Pennemann H, Kolb G. Effect of support and
766 chelating ligand on the synthesis of Ni catalysts with high activity and stability for
767 CO2 methanation. Catalysts 2020;10:493. https://doi.org/10.3390/catal10050493.

768 [41] Rodriguez-Gomez A, Caballero A. Identification of Outer and Inner Nickel
769 Particles in a Mesoporous Support: How the Channels Modify the Reducibility of
770 Ni/SBA-15 Catalysts. ChemNanoMat 2017;3:94–7.
771 https://doi.org/10.1002/cnma.201600297.

772 [42] Everett OE, Zonetti PC, Alves OC, de Avillez RR, Appel LG. The role of oxygen
773 vacancies in the CO2 methanation employing Ni/ZrO2 doped with Ca. Int J
774 Hydrogen Energy 2020;45:6352–9.
775 https://doi.org/10.1016/j.ijhydene.2019.12.140.

776 [43] Wang S, Lu GQM. CO2 reforming of methane on Ni catalysts: Effects of the
777 support phase and preparation technique. Appl Catal B Environ 1998;16:269–77.
778 https://doi.org/10.1016/S0926-3373(97)00083-0.

779 [44] Li J, Lin Y, Pan X, Miao D, Ding D, Cui Y, et al. Enhanced CO2 Methanation
780 Activity of Ni/Anatase Catalyst by Tuning Strong Metal-Support Interactions.
781 ACS Catal 2019;9:6342–8. https://doi.org/10.1021/acscatal.9b00401.

782 [45] Bukhari SN, Chong CC, Teh LP, Vo DVN, Ainirazali N, Triwahyono S, et al.
783 Promising hydrothermal technique for efficient CO2 methanation over Ni/SBA-15.
784 Int J Hydrogen Energy 2019;44:20792–804.
785 https://doi.org/10.1016/j.ijhydene.2018.07.018.

786 [46] Lu B, Ju Y, Abe T, Kawamoto K. Grafting Ni particles onto SBA-15 , and their

enhanced performance for CO2 methanation. RSC Adv 2015;5:56444–54. https://doi.org/10.1039/c5ra07461d.

[47] Zhang S, Muratsugu S, Ishiguro N, Tada M. Supporting Information Ceria-doped Ni / SBA-16 Catalysts for Dry Reforming of Methane n.d.

[48] Wang X, Zhu L, Zhuo Y, Zhu Y, Wang S. Enhancement of CO2 Methanation over La-Modified Ni/SBA-15 Catalysts Prepared by Different Doping Methods. ACS Sustain Chem Eng 2019;7:14647–60. https://doi.org/10.1021/acssuschemeng.9b02563.

[49] Bacariza MC, Graça I, Bebiano SS, Lopes JM, Henriques C. Micro- and mesoporous supports for CO2 methanation catalysts: A comparison between SBA-15, MCM-41 and USY zeolite. Chem Eng Sci 2018;175:72–83. https://doi.org/10.1016/j.ces.2017.09.027.

[50] Guo X, Traitangwong A, Hu M, Zuo C, Meeyoo V, Peng Z, et al. Carbon Dioxide Methanation over Nickel-Based Catalysts Supported on Various Mesoporous Material. Energy and Fuels 2018;32:3681–9. https://doi.org/10.1021/acs.energyfuels.7b03826.

[51] Han Y, Wen B, Zhu M, Dai B. Lanthanum incorporated in MCM-41 and its application as a support for a stable Ni-based methanation catalyst. J Rare Earths 2018;36:367–73. https://doi.org/10.1016/j.jre.2017.07.016.

[52] Wang L, Liu H, Ye H, Hu R, Yang S, Tang G, et al. Vacuum thermal treated Ni-CeO2/SBA-15 catalyst for CO2 methanation. Nanomaterials 2018;8:1–10. https://doi.org/10.3390/nano8100759.

809 [53] Zhou Y, Zhou J. Interactions of Ni nanoparticles with reducible CeO 2(111) thin
810 films. J Phys Chem C 2012;116:9544–9. https://doi.org/10.1021/jp300259y.

811 [54] Daza CE, Moreno S, Molina R. Co-precipitated Ni-Mg-Al catalysts containing Ce
812 for CO2 reforming of methane. Int J Hydrogen Energy 2011;36:3886–94.
813 https://doi.org/10.1016/j.ijhydene.2010.12.082.

814 [55] Świrk K, Rønning M, Motak M, Beaunier P, Da Costa P, Grzybek T. Ce- and Y-
815 Modified Double-Layered Hydroxides as Catalysts for Dry Reforming of
816 Methane: On the Effect of Yttrium Promotion. Catalysts 2019;9:56.
817 https://doi.org/10.3390/catal9010056.

818 [56] Wang N, Chu W, Zhang T, Zhao XS. Synthesis, characterization and catalytic
819 performances of Ce-SBA-15 supported nickel catalysts for methane dry reforming
820 to hydrogen and syngas. Int J Hydrogen Energy 2012;37:19–30.
821 https://doi.org/10.1016/j.ijhydene.2011.03.138.

822 [57] Shanmugam V, Zapf R, Neuberg S, Hessel V, Kolb G. Effect of ceria and zirconia
823 promotors on Ni/SBA-15 catalysts for coking and sintering resistant steam
824 reforming of propylene glycol in microreactors. Appl Catal B Environ
825 2017;203:859–69. https://doi.org/10.1016/j.apcatb.2016.10.075.

826 [58] Yamamoto K, Sunagawa Y, Takahashi H, Muramatsu A. Metallic Ni nanoparticles
827 confined in hexagonally ordered mesoporous silica material. Chem Commun
828 2005;2:348–50. https://doi.org/10.1039/b411074a.

829 [59] Dai B, Wen B, Zhu M, Kang L, Yu F. Nickel catalysts supported on amino-
830 functionalized MCM-41 for syngas methanation. RSC Adv 2016;6:66957–62.

https://doi.org/10.1039/c6ra07451k.

[60] Chen CS, Budi CS, Wu HC, Saikia D, Kao HM. Size-Tunable Ni Nanoparticles Supported on Surface-Modified, Cage-Type Mesoporous Silica as Highly Active Catalysts for CO2 Hydrogenation. ACS Catal 2017;7:8367–81. https://doi.org/10.1021/acscatal.7b02310.

[61] Bian Z, Xin Z, Meng X, Tao M, Lv YH, Gu J. Effect of Citric Acid on the Synthesis of CO Methanation Catalysts with High Activity and Excellent Stability. Ind Eng Chem Res 2017;56:2383–92. https://doi.org/10.1021/acs.iecr.6b04027.

[62] Dong H, Liu Q. Three-Dimensional Networked Ni-Phyllosilicate Catalyst for CO2 Methanation: Achieving High Dispersion and Enhanced Stability at High Ni Loadings. ACS Sustain Chem Eng 2020;8:6753–66. https://doi.org/10.1021/acssuschemeng.0c01148.

[63] Zahra Taherian, Khataee A, Orooji Y. Nickel-based nanocatalysts promoted over MgO-modified SBA-16 for dry reforming of methane for syngas production: Impact of support and promoters. J Energy Inst 2021. https://doi.org/10.1016/j.joei.2021.04.005.

[64] Budi CS, Wu HC, Chen CS, Saikia D, Kao HM. Ni Nanoparticles Supported on Cage-Type Mesoporous Silica for CO2 Hydrogenation with High CH4 Selectivity. ChemSusChem 2016;9:2326–31. https://doi.org/10.1002/cssc.201600710.

[65] Li JF, Xia C, Au CT, Liu BS. Y2O3-promoted NiO/SBA-15 catalysts highly active for CO2/CH4 reforming. Int J Hydrogen Energy 2014;39:10927–40. https://doi.org/10.1016/j.ijhydene.2014.05.021.

[66] Świrk K, Gálvez ME, Motak M, Grzybek T, Rønning M, Da Costa P. Syngas production from dry methane reforming over yttrium-promoted nickel-KIT-6 catalysts. Int J Hydrogen Energy 2019;44:274–86. https://doi.org/10.1016/j.ijhydene.2018.02.164.

[67] Binnemans K, Jones PT, Müller T, Yurramendi L. Rare Earths and the Balance Problem: How to Deal with Changing Markets? J Sustain Metall 2018;4:126–46. https://doi.org/10.1007/s40831-018-0162-8.

[68] Li B, Zhang S. Methane reforming with CO2 using nickel catalysts supported on yttria-doped SBA-15 mesoporous materials via sol-gel process. Int J Hydrogen Energy 2013;38:14250–60. https://doi.org/10.1016/j.ijhydene.2013.08.105.

[69] Świrk K, Gálvez ME, Motak M, Grzybek T, Rønning M, Da Costa P. Syngas production from dry methane reforming over yttrium-promoted nickel-KIT-6 catalysts. Int J Hydrogen Energy 2019;4:274–86. https://doi.org/10.1016/j.ijhydene.2018.02.164.

[70] Sun C, Świrk K, Wang Y, Scheidl KS, Breiby DW, Rønning M, et al. Tailoring the yttrium content in Ni-Ce-Y/SBA-15 mesoporous silicas for CO2 methanation. Catal Today 2021;382:104–19. https://doi.org/10.1016/j.cattod.2021.07.031.

[71] Kim TW, Ryoo R, Kruk M, Gierszal KP, Jaroniec M, Kamiya S, et al. Tailoring the pore structure of SBA-16 silica molecular sieve through the use of copolymer blends and control of synthesis temperature and time. J Phys Chem B 2004;108:11480–9. https://doi.org/10.1021/jp048582k.

[72] Sun C, Świrk K, Wang Y, Scheidl KS, Breiby DW, Rønning M, et al. Tailoring the

yttrium content on Ni-Ce-Y / SBA-15 mesoporous silicas for CO2 methanation. Catal Today 2021. https://doi.org/https://doi.org/10.1016/j.cattod.2021.07.031.

[73] Świrk K, Delahay G, Zaki A, Adil K, Cadiau A. Facile modifications of HKUST-1 by V, Nb and Mn for low-temperature selective catalytic reduction of nitrogen oxides by NH3. Catal Today 2021. https://doi.org/10.1016/j.cattod.2021.07.017.

[74] Stevens WJJ, Lebeau K, Mertens M, Van Tendeloo G, Cool P, Vansant EF. Investigation of the morphology of the mesoporous SBA-16 and SBA-15 materials. J Phys Chem B 2006;110:9183–7. https://doi.org/10.1021/jp0548725.

[75] Kesavan JK, Luisetto I, Tuti S, Meneghini C, Iucci G, Battocchio C, et al. Nickel supported on YSZ: The effect of Ni particle size on the catalytic activity for CO2 methanation. J CO2 Util 2018;23:200–11. https://doi.org/10.1016/j.jcou.2017.11.015.

[76] Matos JR, Kruk M, Mercuri LP, Jaroniec M, Zhao L, Kamiyama T, et al. Ordered mesoporous silica with large cage-like pores: Structural identification and pore connectivity design by controlling the synthesis temperature and time. J Am Chem Soc 2003;125:821–9. https://doi.org/10.1021/ja0283347.

[77] Gobin OC, Wan Y, Zhao D, Kleitz F, Kaliaguine S. Mesostructured silica SBA-16 with tailored intrawall porosity part 1: Synthesis and characterization. J Phys Chem C 2007;111:3053–8. https://doi.org/10.1021/jp0635765.

[78] Kruk M, Hui CM. Thermally induced transition between open and closed spherical pores in ordered mesoporous silicas. J Am Chem Soc 2008;130:1528–9. https://doi.org/10.1021/ja0749035.

[79] Chong CC, Teh LP, Setiabudi HD. Syngas production via CO2 reforming of CH4 over Ni-based SBA-15: Promotional effect of promoters (Ce, Mg, and Zr). Mater Today Energy 2019;12:408–17. https://doi.org/10.1016/j.mtener.2019.04.001.

[80] Cheng MY, Pan CJ, Hwang BJ. Highly-dispersed and thermally-stable NiO nanoparticles exclusively confined in SBA-15: Blockage-free nanochannels. J Mater Chem 2009;19:5193–200. https://doi.org/10.1039/b902949d.

[81] Wagner CD, Passoja DE, Hillery HF, Kinisky TG, Six HA, Jansen WT, et al. Auger and photo-electron line energy relationships in aluminum-oxygen silicon-oxygen compounds. J Vac Sci Technol 1982;21:933–44.

[82] Liu G, Hong G. Synthesis of SiO2/Y2O3:Eu core-shell materials and hollow spheres. J Solid State Chem 2005;178:1647–51. https://doi.org/10.1016/j.jssc.2005.03.010.

[83] Parmigiani F, Depero LE, Sangaletti L, Samoggia G. An XPS study of yttria-stabilised zirconia single crystals. J Electron Spectros Relat Phenomena n.d.;63:1–10.

[84] Wu LQ, Li YC, Li SQ, Li ZZ, Tang GD, Qi WH, et al. Method for estimating ionicities of oxides using O1s photoelectron spectra. AIP Adv 2015;5:097210. https://doi.org/10.1063/1.4931996.

[85] Sohn H, Celik G, Gunduz S, Dogu D, Zhang S, Shan J, et al. Oxygen Mobility in Pre-Reduced Nano- and Macro-Ceria with Co Loading: An AP-XPS, In-Situ DRIFTS and TPR Study. Catal Letters 2017;147:2863–76. https://doi.org/10.1007/s10562-017-2176-4.

[86] R Nyholm and N Martensson. Core level binding energies for the elements Zr-Te (Z = 40-52). J Phys C Solid State Phys 1980;13:L279-84.

[87] Bellido JDA, Assaf EM. Effect of the Y2O3-ZrO2 support composition on nickel catalyst evaluated in dry reforming of methane. Appl Catal A Gen 2009;352:179–87.

[88] Varkolu M, Velpula V, Ganji S, Burri DR, Rao Kamaraju SR. Ni nanoparticles supported on mesoporous silica (2D, 3D) architectures: highly efficient catalysts for the hydrocyclization of biomass-derived levulinic acid. RSC Adv 2015;5:57201–10. https://doi.org/10.1039/c5ra10857h.

[89] Bian Z, Meng X, Tao M, Lv YH, Xin Z. Effect of MoO3 on catalytic performance and stability of the SBA-16 supported Ni-catalyst for CO methanation. Fuel 2016;179:193–201. https://doi.org/10.1016/j.fuel.2016.03.091.

[90] Kirumakki SR, Shpeizer BG, Sagar GV, Chary KVR, Clearfield A. Hydrogenation of Naphthalene over NiO/SiO2-Al2O3 catalysts: Structure-activity correlation. J Catal 2006;242:319–31. https://doi.org/10.1016/j.jcat.2006.06.014.

[91] Selvaraj M, Park DW, Ha CS. Well ordered two-dimensional mesoporous CeSBA-15 synthesized with improved hydrothermal stability and catalytic activity. Microporous Mesoporous Mater 2011;138:94–101. https://doi.org/10.1016/j.micromeso.2010.09.025.

[92] Ashok J, Kathiraser Y, Ang ML, Kawi S. Bi-functional hydrotalcite-derived NiO-CaO-Al2O3 catalysts for steam reforming of biomass and/or tar model compound at low steam-to-carbon conditions. Appl Catal B Environ 2015;172–173:116–28.

941 https://doi.org/10.1016/j.apcatb.2015.02.017.

942 [93] Romero-Sáez M, Dongil AB, Benito N, Espinoza-González R, Escalona N, Gracia
943 F. CO2 methanation over nickel-ZrO2 catalyst supported on carbon nanotubes: A
944 comparison between two impregnation strategies. Appl Catal B Environ
945 2018;237:817–25. https://doi.org/10.1016/j.apcatb.2018.06.045.

946 [94] Dong X, Li F, Zhao N, Xiao F, Wang J, Tan Y. CO2 hydrogenation to methanol
947 over Cu/ZnO/ZrO2 catalysts prepared by precipitation-reduction method. Appl
948 Catal B Environ 2016;191:8–17. https://doi.org/10.1016/j.apcatb.2016.03.014.

949 [95] Pan Q, Peng J, Sun T, Wang SS, Wang SS, Qiushi P, et al. Insight into the reaction
950 route of CO2 methanation: Promotion effect of medium basic sites. Catal Commun
951 2014;45:74–8. https://doi.org/10.1016/j.catcom.2013.10.034.

952 [96] Zeng L, Wang Y, Li Z, Song Y, Zhang J, Wang J, et al. Highly Dispersed Ni
953 Catalyst on Metal − Organic Framework-Derived Porous Hydrous Zirconia for
954 CO2 Methanation. ACS Appl Mater Interfaces 2020;12:17436–42.
955 https://doi.org/10.1021/acsami.9b23277.

956 [97] Świrk K, Gálvez ME, Motak M, Grzybek T, Rønning M, Da Costa P. Yttrium
957 promoted Ni-based double-layered hydroxides for dry methane reforming. J CO2
958 Util 2018;27:247–58. https://doi.org/10.1016/j.jcou.2018.08.004.

959 [98] Wang Y, Yao L, Wang Y, Wang S, Zhao Q, Mao D, et al. Low-Temperature
960 Catalytic CO2 Dry Reforming of Methane on Ni-Si/ZrO2 Catalyst. ACS Catal
961 2018;8:6495–506. https://doi.org/10.1021/acscatal.8b00584.

962